Solvent and Additive Engineering for Low Band Gap Perovskite Solar Cells

Thomas W. Green
St Hilda's College
University of Oxford



Thesis submitted in fulfilment of the requirements for the degree of Master of Science by Research at the University of Oxford.

Hilary Term, 2020

Solvent and Additive Engineering for Low Band Gap Perovskite Solar Cells

Thomas W. Green, St Hilda's College, University of Oxford

Thesis submitted in fulfilment of the requirements for the degree of Master of Science by Research at the University of Oxford. Hilary Term, 2020

Apart from where explicitly stated, all the work presented in this thesis is my own.

Abstract

Due to their tuneable band gaps, ease of processing and excellent optoelectronic properties, perovskite-based solar cells have attracted much attention in recent years, with rapidly increasing efficiencies which already match those of the industrially dominant multi-crystalline silicon. This work concerns modification of the perovskite semiconductor layer in low band gap materials containing the mixed metals tin and lead. These materials have promising commercial applications both in theoretically optimal single-junction solar cells and in multi-junction perovskite-perovskite tandem devices as a replacement for silicon.

An improved processing method by modification of the deposition solvent together with an appropriate antisolvent or stream of nitrogen is shown to slow crystallisation, leading to thin films with long diffusion length and high mobility. Use of a formamidinium cation rather than methylammonium is shown to improve efficiency, with further performance enhancement on substitution of a small amount of caesium. An optoelectronically defective region is identified with small amounts of substitution of lead for tin, with a recovery in film quality and lowest band gap values with 40-60% tin content. In collaboration with others, this processing enhancement leads to high efficiency single-junction low band gap perovskite solar cells and multi-junction perovskite-perovskite tandem devices.

The additives tin(II) fluoride and tin(II) chloride are shown to function as reducing agents in precursor solutions, and compensators in thin films for tin vacancies produced by the instability of tin(II). These additives are able to rebalance the stoichiometry of both tin(II) and iodide, allowing formation of perovskite films with less bulk vacancy defects, leading to improved morphology and optoelectronic quality, and less initial p-doping. A secondary phase seen on the surface of the films is identified as excess tin(II) fluoride. Over time in air, competing p-doping and degradation mechanisms are identified, and additives shown to slow the onset of degradation. High efficiency solar cells are fabricated with both additives, with tin(II) fluoride showing less sensitivity to precise processing concentration.

A compositional screening study of methylammonium, formamidinium and caesium cations in low band gap perovskite materials is performed, identifying thin film properties and fabricating solar cells from compositions with different combinations of these cations using a universal deposition protocol. The resulting compositional space is demonstrated to be almost fully accessible using this method, with all three cations substituting into the perovskite crystal lattice, although a compositional instability between formamidinium and caesium is identified. Power is generated from solar cells of all other compositions, laying the foundations for future optimisation work on new low band gap materials within this compositional space.

List of Publications

1. R.L. Milot, G.E. Eperon, T. Green, H.J. Snaith, M.B. Johnston, L.M. Herz. Radiative Monomolecular Recombination Boosts Amplified Spontaneous Emission in $HC(NH_2)_2SnI_3$ Perovskite Films. *J. Phys. Chem. Lett.* **2016**, *7*, 4178.

2. G.E. Eperon, T. Leijtens, K.A. Bush, R. Prasanna, T. Green, J.T.-W. Wang, D.P. McMeekin, G. Volonakis, R.L. Milot, R. May, A. Palmstrom, D.J. Slotcavage, R.A. Belisle, J.B. Patel, E.S. Parrott, R.J. Sutton, W. Ma, F. Moghadam, B. Conings, A. Babayigit, H.-G. Boyen, S. Bent, F. Giustino, L.M. Herz, M.B. Johnston, M.D. McGehee, H.J. Snaith. Perovskite-perovskite tandem photovoltaics with optimized band gaps. *Science* **2016**, *354*, 861.

3. E.S. Parrott, T. Green, R.L. Milot, M.B. Johnston, H.J. Snaith, L.M. Herz. Interplay of Structural and Optoelectronic Properties in Formamidinium Mixed Tin-Lead Triiodide Perovskites. *Adv. Funct. Mater.* **2018**, *28,* 1802803.

4. M.T. Klug, R.L. Milot, J.B. Patel, T. Green, H.C. Sansom, M.D. Farrar, A.J. Ramadan, S. Martani, Z. Wang, B. Wenger, J.M. Ball, L. Langshaw, A. Petrozza, M.B. Johnston, L.M. Herz, H.J. Snaith. Metal composition influences optoelectronic quality in mixed-metal lead-tin triiodide perovskite solar absorbers. *Energy Environ. Sci.,* **2020**, *13*, 1776.

Table of contents

1. Introduction **5**
1.1 Background and motivation 5
1.2 Aims of this thesis 6
2. Background **7**
2.1 Semiconductors 7
2.2 Solar cell operation 8
2.3 Current-voltage hysteresis 12
2.4 Perovskites 13
2.5 Perovskite solar cell structure and operation 14
2.6 Multi-junction solar cells 15
3. Methods **16**
3.1 Perovskite preparation 16
3.2 Solar cell fabrication 17
3.3 Solar cell characterisation 18
3.4 Optical characterisation 18
3.5 Material characterisation 20
4. Solvent engineering for morphological control and improved performance of formamidinium-based mixed tin-lead perovskite solar cells **21**
4.1 Introduction 21
4.2 Precursor phase antisolvent immersion 21
4.3 $FASn_xPb_{1-x}I_3$ thin film characterisation, single and multi-junction solar cells 24
4.4 Complex-assisted gas quenching 24
4.5 Correlating optoelectronic defectiveness across the full range of (Sn:Pb) content[58] 26
4.6 Conclusion 27
5. The role of additives as reducing agents and tin vacancy compensators in low band gap perovskite solar cells **28**
5.1 Introduction 28
5.2 Effect on solutions 29
5.3 Effect on thin films: SEM, EDX, XRD 30
5.4 Effect on Solar Cell parameters 33
5.5 Trap reduction in films: EQE, THz, TRPL 34
5.6 Trap-reduction in films (time-dependant measurements): conductivity, Kelvin probe 37
5.7 Conclusion 40
6. Organic and inorganic cation screening for mixed tin-lead perovskite solar cells **41**
6.1 Introduction 41
6.2 Substitution of Cs: fabrication of $FA_{1-y}Cs_ySn_xPb_{1-x}I_3$ perovskites 41
6.3 Triple cation perovskites: thin film properties 43
6.4 Triple cation perovskites: solar cells 46
6.5 Conclusion 48
7. Conclusions and outlook **49**
8. References **51**

1. Introduction

1.1 Background and motivation

Research into new energy generation technologies that do not rely on a finite fuel source, nor release greenhouse gases into the atmosphere, is becoming increasingly important in order to combat man-made climate change and the exhaustion of the world's finite fossil fuel supplies. Solar photovoltaics (PV) are the leading candidate for terawatt-scale, low-carbon electricity generation in the world today. The global average solar irradiance over land is 183 Wm^{-2}, and if only a fraction of this incident sunlight could be harvested, enough power could easily be generated to satisfy the world's needs, requiring only 0.4% of the Earth's surface to be covered with devices able to convert 20% of the incident solar energy into power[1]. Although the growth of PV has been rapid in recent years, by April 2019 the cumulative photovoltaic capacity installed was 486GW, still only corresponding to less than 1% of global electricity demand[2].

PV efficiencies are governed by the Shockley-Queisser limit, which states that a maximum power conversion efficiency (PCE) of 33.7% is possible for a single-junction semiconductor device, with optimum band gap of 1.34eV[3]. The most widely deployed PV material in the world today is crystalline silicon, which has an indirect band gap of 1.1eV, and PCE values around 25%. Other wafer-based materials include gallium arsenide (GaAs, 1.42eV band gap, 28% PCE) and III-V multi-junction cells. However, these modules require numerous expensive high temperature processes to manufacture and are bulky and expensive to install. In contrast, thin film solar cells make use of the high absorption coefficients of direct band gap semiconductors to absorb light in films just a few microns across, compared to the hundreds of microns used in wafer-based devices[4]. Commercialised technologies with high efficiencies include cadmium telluride (CdTe) and copper indium gallium (di)selenide (CIGS), both of which have reached 22% PCE[1]. However, these cells often use rare elements which are in short supply, so are not a realistic choice for terawatt-scale production. Devices that can be produced by solution processing (spin coating, blade coating, spraying, inkjet printing, gravure printing, or slot-dye coating) without the need for high temperature processes offer an attractive route for scalable PV technology. Dye-sensitized solar cells (DSSCs)[5], quantum dot solar cells[6], and organic solar cells[7] can all be manufactured in this way, but their theoretical maximum efficiencies are limited by disorder and heterogeneous charge generation processes in the materials, leading to a trade-off between open-circuit voltage and photocurrent generation[8].

In recent years, a new family of solution-processable semiconducting materials based on an organometallic tri-halide perovskite structure have been developed as sensitizers for hybrid solid-state solar cells. These perovskite solar cells have quickly become a promising new photovoltaic technology, with certified efficiencies reaching over 25% after just 10 years of research focus[9]. Their tuneable band gaps, high charge-carrier mobilities, long charge-carrier lifetimes and diffusion lengths, high defect tolerance, and low-cost preparation methods such as solution or vapour deposition mean they are already emerging as a competitive commercial technology[10][11][12][13].

Tuning perovskite semiconductor band gaps by chemical composition allows the materials to be tailored to specific applications[14]. Most work has been focussed on single-junction devices with band gaps around 1.6eV, however, despite their ease of processing, routes to commercial viability for perovskites as single-junction solar devices seem limited, as much as 50-80% of the cost of a solar module can be in the balance-of-systems[1]. Hence it will be difficult for single-junction perovskites to become competitive with the established silicon solar industry. Where perovskites could have an important role to play is in multi-junction tandem devices, where two solar cells with different band gaps absorbing different parts of the solar spectrum are mechanically stacked or processed on top of each other; here the perovskite cell can increase efficiency while only slightly increasing production costs[15]. As the world's population increases and land area becomes a premium, perovskite-perovskite or perovskite-silicon tandem modules will become more and more commercially viable.

1.2 Aims of this thesis

This thesis focuses on perovskites containing tin (Sn) as well as the more usual lead (Pb). Tin substitution into the perovskite structure offers the only known route to achieve band gaps below 1.5eV, including band gaps around the optimal value of 1.34eV for single-junction devices[14]. These low band gap perovskites are also commercially essential as a replacement for silicon in all-perovskite tandem devices. Sn-based perovskites have been investigated alongside Pb-based perovskites since the start of modern research; the first use of a perovskite in a solid state solar cell was in a DSSC using caesium tin iodide ($CsSnI_3$) as a p-type hole transport layer and absorber[16].

Replacing Pb in the perovskite absorber with Sn could also have an environmental advantage, as lead is a toxic material. However, even if all the electricity in the USA were supplied by lead-based perovskite solar panels, the total rate of lead leaching into the environment would still be two orders of magnitude lower than the existing rate of leaching of lead-based solder from used electronic devices[17]. Tin leaching may also result in environmental concerns of its own if not disposed of appropriately[18]. As the lead in perovskite solar modules is in the solid state, encapsulated, and specifically must remain there for the technology to be viable, its toxicity should not be a major concern, as long as appropriate panel recycling techniques are developed alongside the roll out of perovskite PV.

Sn-based perovskites do however exhibit a number of key issues which do not affect Pb-based perovskites, including the instability of tin in its Sn^{2+} state and ready oxidation to Sn^{4+} on exposure to air, and the rapid crystallisation of Sn-containing perovskites during fabrication, leading to poor thin film morphology[19]. These issues have hindered the optoelectronic quality of Sn-based films; efficiencies above 6% have been difficult to achieve until recently[20][21].

This thesis focuses on modification of the perovskite semiconductor layer in mixed Sn-Pb thin films and solar cells. Chapter 4 presents an improved processing technique and use of an alternative organic cation within the perovskite structure to address the rapid crystallisation of Sn-Pb films during fabrication, leading to improved optoelectronic film quality. This processing improvement leads to high performance single-junction low band gap perovskite solar cells, and some of the first all-perovskite multi-junction solar cells[22].

Chapter 5 examines how tin(II) fluoride (SnF_2) and tin(II) chloride ($SnCl_2$) additives can be used to reduce Sn^{2+} vacancies in mixed Sn-Pb perovskites, and how these additives have a function both as reducing agents in precursor solutions and as vacancy compensators within the perovskite thin films. It is shown that additive addition improves the morphology and optoelectronic quality of the perovskite layer; optimised additive concentrations for high performance low band gap solar cells are discussed. Thin films of Sn-Pb perovskites are examined over time in air, and it is shown how additives can affect the balance between p-doping and degradation mechanisms within the films.

A fuller compositional screening study on the effect of organic and inorganic cation choice within Sn-Pb perovskites is presented in chapter 6. Here the perovskite structure is modified further from standard materials than in the previous two chapters, and the thin film properties, band gaps, and applicability to solar cells of new low band gap materials containing combinations of the organic and inorganic cations methylammonium, formamidinium and caesium are examined. It is demonstrated that these three cations when used within the Sn-Pb perovskite system produce an almost fully accessible compositional space, and that all compositions can be fabricated by a simple universal deposition protocol. Solar cells of each composition are demonstrated, acting as a proof of concept for future work on new materials within this compositional space, and providing potential routes to even higher performance low band gap perovskite solar cells.

2. Background

This chapter presents a summary of core concepts in semiconductor physics, solar cell operation, perovskites, and perovskite solar cells[4].

2.1 Semiconductors

A solid material with a repeating structure has atomic orbitals arranged in a periodic array. Solving Schrödinger's equation for this array gives rise to a periodic probability distribution of electrons, with the delocalised electrons forming bands. The electron waves effectively diffract from the periodic lattice, and at some points cancel each other out, leading to regions of energy where no electron states are allowed. These regions are called band gaps.

The Fermi level (E_F) of a material is the hypothetical energy level of an electron such that at thermodynamic equilibrium this energy level would have a 50% probability of being occupied at any given time. Metals are good conductors because the Fermi level lies within a band with delocalised electron states, meaning there are a large number of states available to carry current. In an insulator, the Fermi level lies within a large band gap with no available states for conduction at this energy, so insulators cannot carry current. A semiconductor has a band gap which is smaller than that of an insulator (practically, less than around 3eV), so electrons can be excited by energy from heat or light to cross the band gap and conduct. The deeper (lower energy) band is termed the valence band and the higher band the conduction band. The work function of a material is the thermodynamic work required to remove an electron from a point within a material to a point immediately outside the solid surface, so from E_F to the vacuum level E_{vac}.

The band gap represents the minimum energy required to excite an electron up to a state in the conduction band, where it can move freely through the material. In solar cells, a photon from the Sun that is incident on the semiconductor transfers its energy to an electron. The electron is excited to the conduction band, and an electron from an adjacent atom can occupy the space left behind; this hole moves through the crystal in a chain reaction of electron movement that makes the hole act as a free positively charged particle in the valence band, just like the negatively charged electron in the conduction band.

Doping a semiconductor is a process where impurities with different numbers of valence electrons are added to the core material, allowing electrons or holes to be freed more easily from these impurities. This effectively adds electrons or holes to new levels near the conduction or valence bands, thus shifting the position of the Fermi level within the band gap. Adding a material with too many electrons is called n-doping, which adds a donor level near to the conduction band and shifts E_F between this new level and the conduction band. This makes the material more conductive for electrons. Adding a material with too few electrons is essentially adding holes and is called p-doping, which adds an acceptor level near to the valence band and shifts E_F between this new level and the valence band. This makes the material more conductive for holes.

Defects play a central role in semiconductor quality and solar cell operation. Unwanted levels can be created in the band gap due to vacancies, broken bonds, impurities, or grain boundaries (especially in a polycrystalline semiconductor). These can often act as centres for recombination of electrons and holes, or they can act as trap states, capturing a free electron or hole which can either eventually escape, or recombine at this trap level. Trap states therefore decrease the mobility and diffusion length of charge carriers through the semiconductor and decrease optoelectronic quality.

2.2 Solar cell operation

When light is incident on a semiconductor, the energy from a photon can be absorbed by an electron, which is excited to the conduction band, leaving a hole in the valence band. Photons incident on a semiconductor with energy exactly equal to the band gap energy (E_g) promote an electron to the conduction band with no excess energy loss. Photons with more energy than E_g promote an electron to a level higher than the band gap; the electron then thermalises to the band edge, losing the excess energy as heat. Photons with less energy than E_g are not absorbed as they do not have enough energy to promote an electron to the conduction band. Photon energy E is inversely proportional to wavelength λ ($E = hc/\lambda$ where h is Planck's constant and c is the speed of light in vacuum), so semiconductors with a certain band gap cannot absorb light above a certain wavelength.

How much light can be absorbed by a semiconductor is dependent on the array of energies (spectrum) of the light incident upon it. The solar spectrum is different depending on when and where on the Earth's surface it is measured, so it is useful to define a fixed reference, called the Air Mass 1.5 spectrum (AM1.5). This represents the overall yearly average spectrum for mid-latitudes, where most of the Earth's population centres are based, and has become the standardised spectrum for testing of PV devices. A standard total irradiance is also required, set at 100mWcm^{-2}. **Fig. 2.1** shows the AM1.5 spectrum, with shaded sections representing the photons that can be absorbed by a material of band gap 1.22eV (corresponding to a wavelength of 1020nm).

However, in a finite length of semiconductor, not all photons of energy >E_g will be absorbed. The absorption coefficient of a material is how effectively photons are absorbed per unit length and depends on the energetic shape of the density of states. The External Quantum Efficiency, $EQE(\lambda)$ is the ratio of the number of charge carriers collected by the solar cell to the number of incident photons of a given energy, and combines absorption, charge separation and charge collection processes within the semiconductor. The ideal $EQE(\lambda)$ is a step function at the wavelength corresponding to the band gap of the absorber, meaning all photons above band gap energy are absorbed, but in practice $EQE(\lambda)$ is a more complex shape depending on the loss mechanisms in the material.

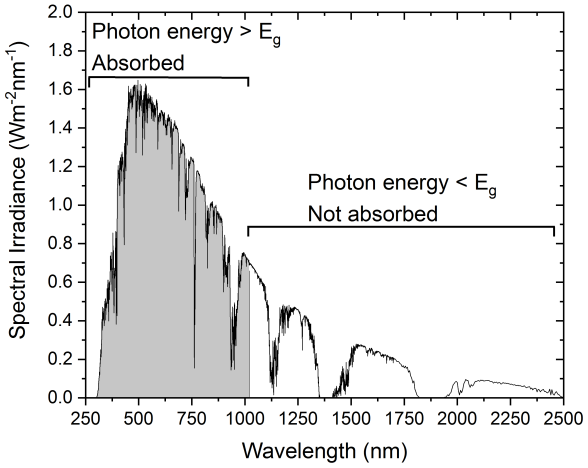


Figure 2.1: AM1.5 standard solar irradiance spectrum, with shaded section showing photons absorbed by a semiconductor of band gap 1.22eV.

Photoinduced charges can be induced to flow out of a semiconductor material by creating some kind of asymmetry in the device structure, such as a p-n junction in the case of silicon solar cells, or n-type and p-type selective contacts in the case of perovskite solar cells, discussed in section 2.5. In general terms, a solar cell is a device which generates current I (usually expressed as current density J, current per unit area) and voltage V under illumination. Under an applied load R, the current density - voltage (J-V) relation *J(V)=V/R* describes how a particular solar cell behaves. The short-circuit current density J_{sc} is the maximum current produced when the two terminals are directly connected (no load), and the open-circuit voltage V_{oc} is the maximum voltage produced when the terminals are isolated (infinite load).

The photon flux distribution (photons per unit area per unit time) as a function of wavelength is given by dividing the AM1.5 spectral irradiance $\Phi_{AM1.5}$ by the energy of each photon $E = hc/\lambda$. The current density as a function of photon wavelength is therefore given by the photon flux multiplied by the charge of an electron, q, modified by the EQE at that wavelength. The total short-circuit current density J_{sc} of a solar cell is given by integrating the AM1.5 photon flux distribution over all wavelengths, modified by the EQE.

$$J_{sc} = q \int EQE(E)\Phi_{AM1.5}(E)dE \quad 2.1$$

$$= q \int EQE(\lambda)\Phi_{AM1.5}(\lambda)\frac{\lambda}{hc}d\lambda \quad 2.2$$

With a 100% EQE, the 1.22eV material shown in **Fig. 2.1** would generate a J_{sc} of 39.2mAcm^{-2}. J_{sc} represents the maximum possible flow of charge carriers in the circuit for a particular material and light source. J_{sc} decreases with increasing band gap as fewer photons excite charge carriers that can flow in the circuit, and it also depends strongly on the spectrum of the incident light, if not standardised to AM1.5. Non-optimum charge collection modifies the EQE away from a step function and decreases J_{sc}.

Incidence of light on a semiconductor creates excess carriers which disturb the semiconductor from thermal equilibrium. As the in-band thermal relaxation processes are fast relative to between-band processes, the carriers can be approximated to be in equilibrium within the bands but not between bands, and quasi-Fermi levels E_{Fn} and E_{Fp} can be defined to represent the average energy of the carrier populations within the bands in quasi-equilibrium.

Fig. 2.2a-b show the energy levels of a semiconductor before and after contact with n and p type layers in dark conditions with no applied bias. In this case, E_F equilibrates along the complete device. As the n-type and p-type layers have low and high work functions, the equilibration produces a built-in potential V_{bi} and corresponding electric field.

Fig. 2.2c-d show the energy levels of this ideal device under illumination at short circuit (no applied bias) and open circuit. At open circuit, application of a voltage V_{oc} produces an electric field such that current flow is stopped. The energy difference between the quasi-Fermi levels in the absorber is the maximum energy that can be converted from radiation into electrochemical energy at the contacts; across the full device the maximum energy that can be extracted (qV_{oc}) will be lower than the quasi-Fermi level splitting due to losses in the transport layers or at the contacts. In an ideal device, V_{oc} increases with increasing band gap as the energy of each charge carrier increases due to increased quasi-Fermi level splitting.

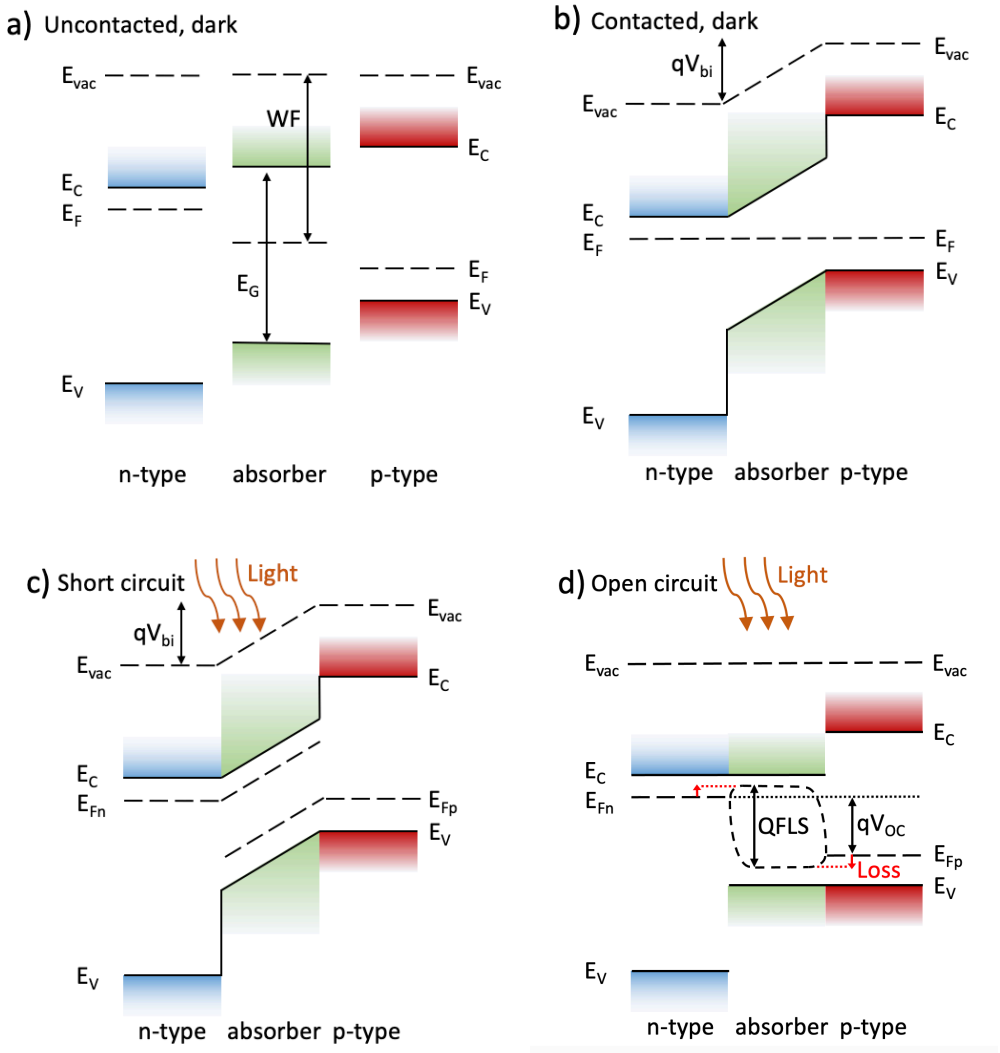


Fig. 2.2: Energy band diagram of a p-i-n solar cell a) in the dark with no contact between materials. b) in the dark contacted, showing equilibration of Fermi level. c) under illumination at short circuit. d) under illumination at open circuit. E_{vac}, E_C, E_V, E_F, E_{Fn}, and E_{Fp}, are the energy levels of vacuum, the conduction band, the valence band, the Fermi level, the quasi Fermi level for electrons, and the quasi Fermi level for holes, respectively; q is the electron charge, V_{bi} is the built-in potential, V_{oc} is the open-circuit voltage and QFLS the quasi-Fermi level splitting.

When under load, a solar cell generates a voltage, causing some charges to flow in the opposite direction to the photocurrent. At V_{oc}, this reverse current is equal to the forwards photocurrent, resulting in net zero current flow. This reverse current or "current in the dark" J_{dark} will flow even with no incident light on the material. Due to the asymmetric device structure, the solar cell behaves like a diode in the dark, allowing charge to flow in one direction only, so the current in the dark can be modelled by an ideal diode equation:

$$J = J_{sc} - J_{dark} \tag{2.3}$$

$$= J_{sc} - J_0\left(\exp\left[\frac{qV}{k_B T}\right] - 1\right) \tag{2.4}$$

where k_B is the Boltzmann constant, T is the temperature in kelvin, and the "dark saturation current" J_0 is a constant for a particular device at a particular temperature which depends on recombination, representing leakage of carriers in the dark across the asymmetry in the device structure.

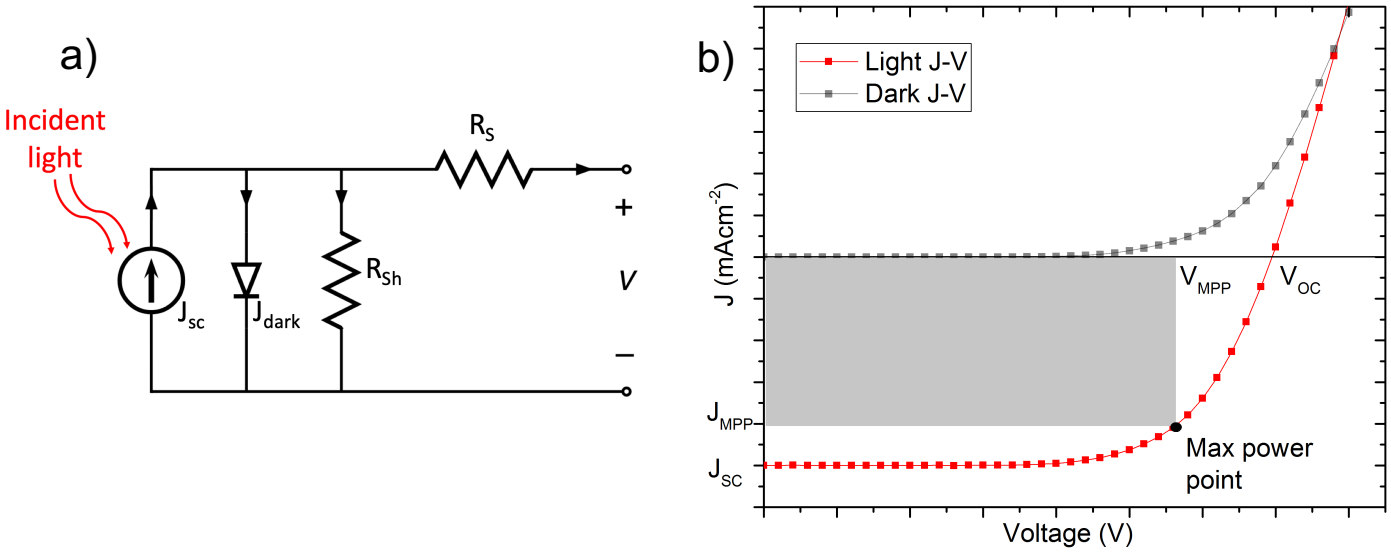


Figure 2.3: a) Equivalent circuit diagram for a solar cell. b) Example current density - voltage (J-V) curve in light and dark, with the maximum power attainable represented by the shaded area.

The ideal diode equation assumes all charge recombination occurs radiatively (band to band) in the bulk areas of the device. In a real material, recombination can occur in other ways, including trap-assisted Shockley-Read-Hall recombination or Auger recombination, so it is common to introduce an "ideality factor" n to modify the equation to account for these, with values of n between 1 and 2 depending on the number of carriers involved in the relevant recombination mechanism.

In addition, parasitic resistances effect the J-V characteristics, and can be split into two types. Series resistance R_S arises from current flow through the bulk materials and from contact resistance between solar cell layers. Shunt resistance R_{Sh} arises from manufacturing defects such as pinholes and recombination at contacts. This leads to a more realistic J-V relation for a solar cell, where A is the device area:

$$J = J_{sc} - J_0\left(\exp\left[\frac{q(V + JAR_S)}{nk_BT}\right] - 1\right) - \frac{V + JAR_S}{R_{Sh}} \qquad 2.5$$

Fig. 2.3a shows the equivalent circuit for equation 2.5, with J_{sc} represented by a photocurrent generating source, J_{dark} represented by a diode with current flowing in the opposite direction, and resistors in series and parallel representing the series and shunt resistances respectively.

Fig. 2.3b shows a typical solar cell J-V curve in the light and dark. Power density $P = JV$ is generated at all points from V = 0 to V_{oc}, corresponding to J = J_{sc} to 0. The maximum power point P_{MPP} is the point at which this product JV (the area under the curve) is at a maximum, occurring at a particular voltage V_{MPP} and current density J_{MPP}. The ratio of P_{MPP} to the theoretically ideal power density $J_{sc}V_{oc}$ is given by the "fill factor" FF, describing the "squareness" of the J-V curve:

$$FF = \frac{J_{MPP}V_{MPP}}{J_{sc}V_{oc}} \qquad 2.6$$

The FF gives an idea of how close the photovoltaic device is functioning to the ideal. Depending on the solar cell architecture, the FF will be decreased by recombination within the device, low shunt resistances, or high series resistances.

The Power Conversion Efficiency (PCE) is defined as the ratio of the power density produced at the maximum power point, to the incident light power density:

$$PCE = \frac{P_{MPP}}{P_{incident}} = \frac{J_{MPP}V_{MPP}}{P_{incident}} = \frac{J_{sc}V_{oc}FF}{\phi A} \quad 2.7$$

Where ϕ represents incident light intensity, set as 100mWcm^{-2} under standard test conditions, and A the cell area. The key performance parameters for a solar cell are J_{sc}, V_{oc}, FF and PCE, which can be extracted from the J-V curve. Solar cell J-V curves are measured under a standard AM1.5 light source by sweeping an applied bias voltage over the terminals of the cell and measuring the resulting current flowing in the external circuit.

Increasing light intensity past AM1.5 increases the "number of suns" incident on the device, important in real world applications such as solar concentrators. As the total number of overall photons of all wavelengths increases, J_{sc} also increases linearly. At high light intensity the series resistance has a greater effect on FF and performance, and at low light intensity the shunt resistance has a greater effect.

Increasing temperature from standard AM1.5 operating conditions generally both decreases the band gap of a semiconductor, and also gives each electron in the material more energy, increasing its likelihood of being excited into the conduction band. Both these effects lead to an increase in intrinsic carrier concentration, which affects the dark saturation current J_0 in equation 2.5. This temperature dependence of J_0 leads to a decrease of V_{oc} with temperature.

2.3 Current-voltage hysteresis

Perovskite solar cells are unusual in that different J-V curves can be observed when the voltage is swept in different directions, either from forward bias V=0 to short circuit J=0 (FB-SC), or from short circuit to forward bias (SC-FB). This J-V hysteresis can lead to one scan direction giving better performance than the other. Hysteresis can arise in silicon-based solar cells as a residual capacitance if the voltage sweep is done too rapidly, however perovskite solar cells can show significant hysteresis effects even at very slow scan speeds.

Perovskites are distinct from many other semiconductors as they exhibit characteristics of both electronic and ionic motion. Hysteresis effects in perovskite solar cells originate from a combination of ion migration throughout the perovskite and electronic charge traps serving as recombination centres[23][24]. Depending on the history of the biasing conditions, this combination can result in a significant loss in photocurrent due to trap-assisted recombination at the perovskite charge collection layer interface. Reducing the density of mobile ionic species, or the carrier trapping at the interface will reduce hysteresis effects.

It has become standard to define a "stabilised power output" SPO as well as PCE for perovskite solar cells, as a measure of hysteresis in the device[23]. After an initial J-V sweep to determine the maximum power point, the device is held at V_{MPP} for a period of time (usually 20-30s) until the current density stabilises; the efficiency at this stabilised current density is called the SPO. While maximum power point tracking could provide a more accurate approximation of efficiency under working conditions, the SPO remains a useful performance parameter for perovskite solar cells.

2.4 Perovskites

A perovskite is any material with the same crystal structure as calcium titanate, $CaTiO_3$. Their general structure is of the form ABX_3, where A and B are two differently sized cations (A larger than B), and X is an anion. In organometal halide perovskites, A is usually the organic cation methylammonium $CH_3NH_3^+$ (MA), formamidinium $CH(NH_2)_2^+$ (FA) or the inorganic caesium Cs^+ cation, B is a divalent metal such as Pb^{2+} or Sn^{2+}, and X is a halide I^-, Br^- or Cl^-. **Fig. 2.4a** shows the ABX_3 structure of the perovskite lattice and **Fig. 2.4b** the chemical structures of the three main A-site cations.

The simplest possible ABX_3 perovskite consists of a high-symmetry cubic structure belonging to the space group $Pm\bar{3}m$. In this structure the halogen anions X occupy the vertices of regular corner-sharing BX_6 octahedra, while the divalent metal cations B sit at the centres of the octahedra. The cavity enclosed by these octahedra contains the monovalent cation A. All the other possible perovskite structures can be obtained by rotating or distorting the BX_6 octahedra, displacing the B metal atoms off-centre or rotating the A cations within the cavity.

Examining the band structure of these materials, the electronic states at the top of the valence bands are of halide p-character, while those at the bottom of the conduction band are mainly derived from the metal p states[25][26]. The organic A cation does not play a major role in determining the band structure, but its size causes the lattice to expand or contract and causes bending of the X-B-X bond angle, changing the optical band gap without affecting the valence band maximum. Alternatively, changing the B-X bond by substituting the metal or halide influences the band gap largely by altering the valence band maximum directly.

There is a relatively small size range allowed for the effective radius of the A-site cation as it has to fit between the BX_6 octahedra; this range is given by the Goldschmidt tolerance factor[27]. The effective ionic radius of MA is 217pm, FA 253pm, and Cs 167pm[27]. The slightly bigger size of the FA cation compared to MA pushes the usually tetragonal $MAPbI_3$ perovskite structure towards the cubic phase, with straighter bond angles and more space inside the cavity.

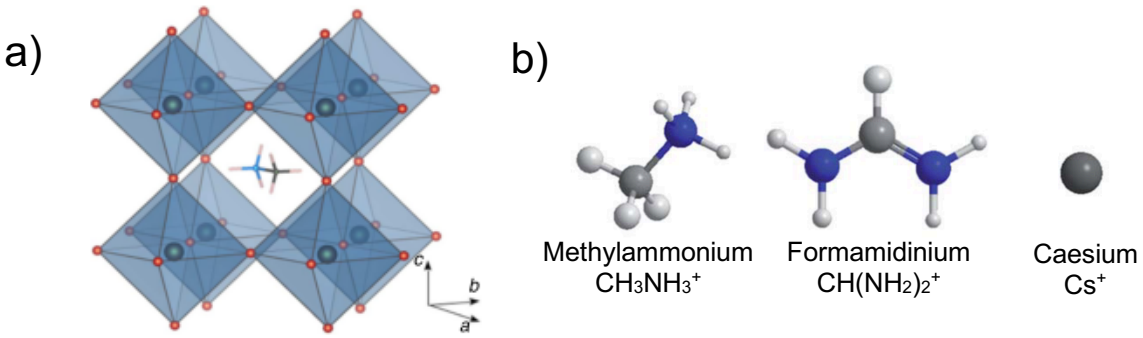


Figure 2.4: a) The ABX_3 chemical structure of perovskites, showing the central (usually organic) cation A^+, metal cation B^{2+} (grey) and octahedral-sharing halide anions X^- (red). b) The chemical structure of the two main organic cations methylammonium $CH_3NH_3^+$ and formamidinium $CH(NH_2)_2^+$, made up of carbon (grey), nitrogen (blue) and hydrogen (white), and the main inorganic cation caesium Cs^+ (grey). Reproduced with permission from ref[28].

The FA cation has a number of advantages over MA. Firstly, $FAPbI_3$ has a slightly smaller band gap of 1.48eV compared to 1.55eV for $MAPbI_3$, which is closer to the optimal Shockley–Queisser limit value of 1.34eV[3]. The absorption edge of FA is at 840nm compared to 800nm for MA; cells based on FA should therefore give a gain of >10% in the photocurrent density compared to MA. FA perovskites also exhibit increased thermal stability at >150°C for long periods, and are more photostable under continual operation; they do not undergo a phase transition in the solar cell operating regime unlike MA, which transitions from the tetragonal to cubic phase at 330K[29], a reachable operating temperature in commercial photovoltaic arrays. The Cs cation is smaller than both FA and MA, and perovskites such as $CsPbI_3$ with a 1.73eV band gap exhibit even better thermal stability than those with organic cations[30].

Changing the X-site halide anion from I^- to Br^- can increase the band gap of the perovskite material[28][31][32]. In mixed-halide perovskites, photoexcitation can cause halide segregation into iodide-rich and bromide-rich regions within the perovskite, with the former acting as recombination centre traps[33]. By substituting MA with a mixture of FA and Cs cations, this phase instability can be removed; $FA_{0.83}Cs_{0.17}(I_{0.6}Br_{0.4})_3$ is a compositionally stable 1.74eV band gap absorber, suitable for the top cell in perovskite-silicon and perovskite-perovskite tandem devices[34].

Replacement of Pb^{2+} at the B-site by Sn^{2+} is the only known method to lower the perovskite band gap below 1.5eV for $MAPbI_3$. Partial replacement with Sn^{2+} leads to anomalous band gap bending with a minimum band gap at almost 1.2eV at 40-60% lead content, lower than that of the end point of $MASnI_3$ which has a 1.4eV band gap[22][35]. First-principles calculations of band gaps as a function of the tin-lead ratio have shown that this band gap bending is likely to be due to a local short-range ordering of the tin or lead-containing octahedra[22]. Fabricating low band gap mixtures of Pb and Sn is a major focus of this thesis and will be discussed in further chapters.

2.5 Perovskite solar cell structure and operation

The first perovskite solar cell studied was in a sensitized architecture, similar to a dye-sensitized solar cell, with the perovskite as the light absorber but the majority of charge transport in other materials, using a mesoporous conducting scaffold such as titanium dioxide (TiO_2)[36]. A first key breakthrough was replacing mesoporous TiO_2 with insulating mesoporous aluminium oxide (Al_2O_3) to create a "meso-superstructured" solar cell (MSSC), with both the charge generation and extraction occurring in the perovskite[37]. The structure of a typical MSSC is shown in **Fig. 2.5a**. Thin-film planar cells do not have any sort of scaffold but a thick layer of perovskite, requiring exact processing conditions to produce high crystallinity[38][39]. In the "regular" structure planar architecture, light enters the perovskite absorber through the electron transporting material (ETM), whereas in the "inverted" structure planar architecture, light is shone through the hole transporting material (HTM).

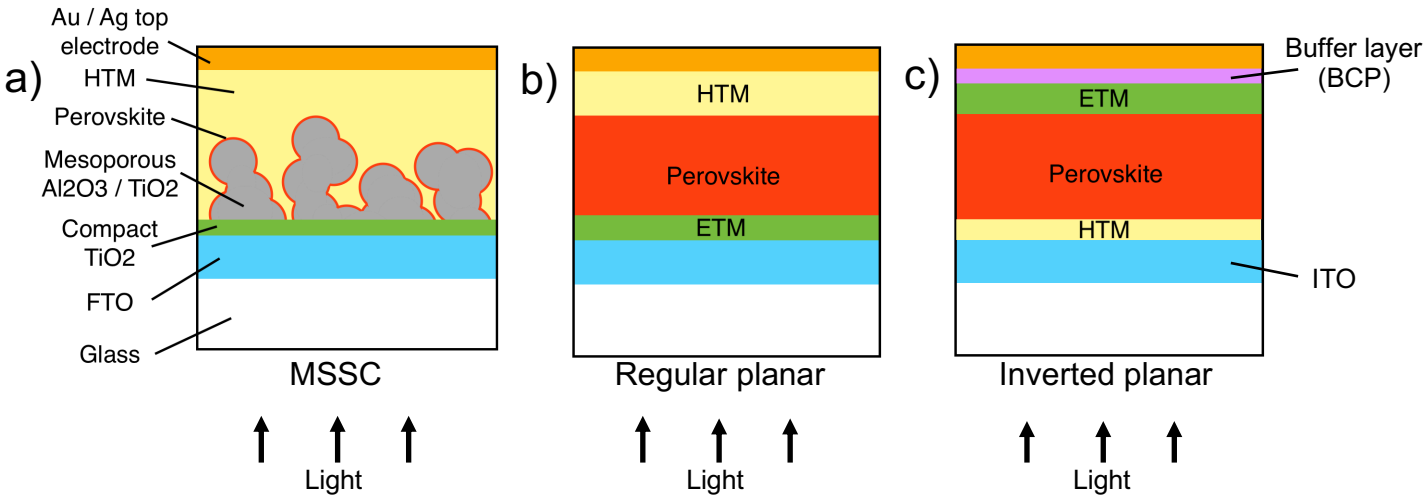


Figure 2.5: Structure of perovskite solar cells: a) Sensitized architecture using either mesoporous TiO_2 or Al_2O_3 (MSSC) b) "Regular" planar solar cell. c) "Inverted" planar solar cell.

Fig. 2.5b shows the structure of a typical regular planar solar cell, consisting of fluorine doped tin oxide (FTO) glass, an ETM such as a TiO_2 compact layer which has been sintered to increase conductivity, the perovskite layer, a HTM such as 2,2′,7,7′-Tetrakis[N,N-di(4-methoxyphenyl)amino]-9,9′-spirobifluorene (Spiro-OMeTAD), and electrodes made of silver (Ag) or gold (Au). **Fig. 2.5c** shows the structure of a typical inverted structure planar solar cell, consisting of indium doped tin oxide (ITO) glass, a HTM such as Poly(3,4-ethylenedioxythiophene)-poly(styrenesulfonate) (PEDOT:PSS), the perovskite layer, an ETM such as phenyl-C_{61}-butyric acid methyl ester (PCBM), a buffer layer of bathocuproine (BCP), and Au or Ag electrodes.

The operating principles of a perovskite solar cell are straightforward. When light is absorbed in the perovskite, electrons and holes are excited into the conduction and valence bands respectively, separate immediately due to the low exciton binding energy, and diffuse around the material[40]. The selective contacts create an asymmetric structure. When a charge carrier reaches the correct selective contact (HTM or ETM), it is immediately extracted and travels through the selective material to the electrode, creating a current. Carriers reaching the incorrect selective contact are energetically blocked from being extracted, so current flows in one direction.

2.6 Multi-junction solar cells

Due to their tuneable band gaps and ease of processing, one of the most promising commercial applications of perovskites is in the fabrication of multi-junction solar cells, where two or more absorber materials with different band gaps are stacked on top of each other, each harvesting different fractions of the solar spectrum, so absorbing more photon energy than is possible in a single-junction device. Modelling has shown that perovskite-perovskite and perovskite-silicon double-junction cells could both feasibly approach 32% PCE, all-perovskite triple-junction cells could reach 33% and perovskite-perovskite-silicon triple-junction cells could surpass 35%[15][41].

Fabrication of multi-junction cells is not trivial; care must be taken to minimise any parasitic absorption and thin film interference effects, as well as matching and maximising light absorption in each absorber layer. Each subcell in a multi-junction device filters light out from the cells beneath it. There are two main architectures for multi-junction cells: 2-terminal devices are processed directly on top of each other, but the subcells must be current matched to deliver optimum performance and connected with a recombination layer, such as sputtered ITO. 4-terminal devices operate the two cells independently, allowing different current densities in each device, but require an extra transparent electrode which can result in more absorption losses and higher cost. 3-terminal tandem devices have also been fabricated; like the 2-terminal case these are monolithic devices featuring a contact shared by both subcells, allowing a combined current density, but with the subcells able to be operated individually at their maximum power points, like the 4-terminal case[42]. **Fig. 2.6** shows the structure of 2-terminal and 4-terminal tandem devices.

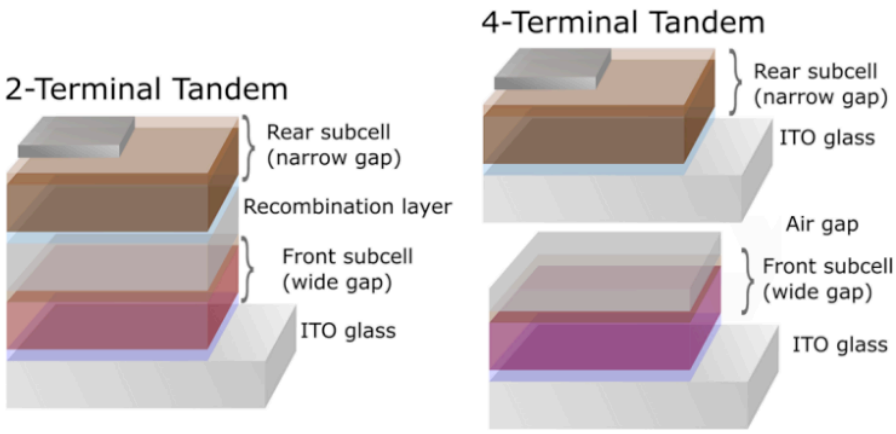


Figure 2.6: Structure of 2-terminal and 4-terminal tandem solar cell devices. Reproduced with permission from ref[22].

3. Methods

This chapter outlines the preparation, fabrication and characterisation techniques used in this thesis.

3.1 Perovskite preparation

Unless otherwise stated, chemicals were purchased from Sigma-Aldrich or Alfa Aesar and used as received. Tin-based precursors were never knowingly exposed to air and all solutions were prepared in a nitrogen-filled glovebox. The methods below result in perovskite film thicknesses of 250-350nm.

3.1.1 $FASn_xPb_{1-x}I_3$ and $(FA:MA:Cs)Sn_xPb_{1-x}I_3$ precursor solution preparation

For $FASn_xPb_{1-x}I_3$ perovskite, precursor solutions of $FASnI_3$ and $FAPbI_3$ were prepared at a concentration of 0.75-1M in a mixed solvent of anhydrous *N,N*-dimethylformamide (DMF) and anhydrous dimethylsulfoxide (DMSO) with a DMF:DMSO ratio of 65:35 by volume. The solutions were dissolved at 1:1 by moles FAI to SnI_2/PbI_2. In addition, excess SnF_2 or $SnCl_2$ powder was added into the tin precursor at various molar excesses (e.g. 0.2M providing a 20% molar excess of tin). In chapters 4 and 6, 10% molar excess of SnF_2 was used as standard. The Sn and Pb precursors were then mixed in the appropriate ratio before spin coating.

For $(FA:MA:Cs)Sn_{0.5}Pb_{0.5}I_3$ perovskite, precursor solutions of $FASn_{0.5}Pb_{0.5}I_3$, $MASn_{0.5}Pb_{0.5}I_3$ and $CsSn_{0.5}Pb_{0.5}I_3$ were prepared at a concentration of 0.75M in the mixed DMF:DMSO solvent in a similar manner as described above, with a 10% molar excess of SnF_2. Solutions were then mixed in order to create the appropriate ratios of cations.

3.1.2 $FASn_xPb_{1-x}I_3$ film formation: precursor phase antisolvent immersion method

For $FASn_xPb_{1-x}I_3$ perovskite, 100µl of the precursor solution made by mixing the Sn and Pb precursors prepared as described above was spin coated dynamically (dispensed from a pipette onto a spinning substrate), with a substrate speed of 5000rpm for a duration of 1s in a nitrogen-filled glovebox, forming a wet transparent film. This film was then immediately immersed into a small petri dish containing an appropriate antisolvent such as anisole for ~5s, forming a reddish or transparent precursor film. This film was taken out of the anisole and blow-dried with a nitrogen gun before annealing at 70°C for 20 minutes. For the pure Pb films, annealing at 170°C for 10 minutes was necessary to form the black phase perovskite; it formed the yellow phase when heated only at 70°C.

3.1.3 $FASn_xPb_{1-x}I_3$ and $(FA:MA:Cs)Sn_xPb_{1-x}I_3$ film formation: complex-assisted gas quenching method

For $FASn_xPb_{1-x}I_3$ perovskite, 100µl of the precursor solution made by mixing the Pb and Sn precursors prepared as described above was spin coated statically (dispensed from a pipette onto a stationary substrate before spinning), with a 6s ramp and substrate speed of 4000rpm for a duration of 36s in a nitrogen-filled glovebox. After 12s of spinning, nitrogen gas was blown onto the substrate for a further 16s, forming a reddish or transparent precursor film on the spin coater. This film was annealed at 70°C for 20 minutes. For $(FA:MA:Cs)Sn_{0.5}Pb_{0.5}I_3$ perovskites as described in chapter 6, the parameters of initial spin time, N_2 gas quench time, and the anneal time were optimised as shown in **Table 3.1**.

Perovskite formula	Abbreviation	Spin time (s)	Quench time (s)	Anneal time at 70°C (min)
$FASn_{0.5}Pb_{0.5}I_3$	FA	12	16	20
$MASn_{0.5}Pb_{0.5}I_3$	MA	12	16	0
$CsSn_{0.5}Pb_{0.5}I_3$	Cs	12	16	20
$FA_{0.5}MA_{0.5}Sn_{0.5}Pb_{0.5}I_3$	FA-MA	12	16	0
$FA_{0.5}Cs_{0.5}Sn_{0.5}Pb_{0.5}I_3$	FA-Cs	No N_2	No N_2	1
$MA_{0.5}Cs_{0.5}Sn_{0.5}Pb_{0.5}I_3$	MA-Cs	16	20	1
$FA_{0.33}MA_{0.33}Cs_{0.33}Sn_{0.5}Pb_{0.5}I_3$	FA-MA-Cs	12	12	20

Table 3.1 Optimised thin film deposition parameters for $(FA:MA:Cs)Sn_{0.5}Pb_{0.5}I_3$ using a complex-assisted gas quenching method.

3.2 Solar cell fabrication

3.2.1 Substrate preparation
Patterned ITO substrates (Colorado Concept Coatings LLC, ~20$\Omega\square^{-1}$) were cleaned through a sequential process of sonication in a soap solution (2% hellmanex detergent in water), rinsing with deionized water, acetone, and isopropanol. The residual solvent was dried off the substrate by a stream of compressed air (departmental supply). Immediately prior to spin coating the device layers, the cleaned substrates were subjected to treatment with oxygen plasma for 20 minutes.

3.2.2 Hole transporting material (HTM) deposition
For the electron-blocking p-type collection layer, Poly(3,4-ethylenedioxythiophene)-poly(styrenesulfonate) (PEDOT:PSS) (Heraeus Al4083) was dissolved 1:2 in methanol, filtered through a 0.45μm syringe filter (Pall Corp. Acrodisc Supor membrane) and warmed to room temperature. The solution was spin coated dynamically at 4500rpm over 40s in air, before annealing at 150°C for 10min, resulting in a 35nm thick film.

For conductivity samples, Poly[bis(4-phenyl)(2,4,6-trimethylphenyl)amine (PTAA) of thickness 15nm was deposited by by statically dispensing 200 μL of a filtered (200 nm PTFE) solution (1 mg/mL PTAA in toluene) at 4000rpm for 30s with a 4s ramp in air, followed by annealing at 130°C for 10 minutes.

The substrates were then transferred into a nitrogen-filled glove box for the remainder of device processing.

3.2.3 Electron transporting material (ETM) deposition
For the hole-blocking n-type collection layer, a Phenyl-C_{61}-butyric acid methyl ester (PCBM) layer of thickness 20nm was deposited by dynamically dispensing 50 μL of a warm solution (20 mg/ml PCBM in 3:1 chlorobenzene:dicholorobenzene by volume, 90°C) onto pre-warmed perovskite substrates (90°C) and spin coating at 2000rpm for 30s in a nitrogen-filled glovebox. The PCBM layers were annealed at 90°C for 5 minutes.

Once cooled to room temperature, a 5nm thick buffer layer of bathocuproine (BCP) was deposited by dynamically dispensing 70μL of solution (0.5mg/ml BCP in IPA) and spin coating at 4000rpm for 20s without any post-anneal.

3.2.4 Contact deposition
A 100nm thick Ag or Au electrode was thermally evaporated onto the device under vacuum of 10^{-6} Torr at a rate of ~0.1nm/s to complete the devices.

3.2.5 Multi-junction solar cells
Perovskite-perovskite multi-junction solar cells were fabricated by collaborators at Stanford. Fabrication methods can be found in the published work[22].

3.3 Solar cell characterisation

3.3.1 Current density - voltage (J-V) characterisation

J-V curves of solar cell devices were measured in air directly after removal from nitrogen, under a solar simulator (Abet Class AAB sun 2000) generating an AM1.5 solar spectrum at 100 mWcm^{2-} irradiance, with intensity calibrated with a KG2 filtered Si reference cell (NREL calibrated). The spectral mismatch factor, correcting for both the mismatch between the spectral response of the test and reference cells and between the illumination source and the AM 1.5G reference spectrum, was calculated to be less than 1%[43]. The solar cell devices were masked with a 0.0919cm^2 metal aperture to ensure a consistent active area and eliminate edge effects[44]. Each device was measured using a Keithley 2400 source meter. In order to quantify hysteresis in the devices, J-V scans were performed from forward bias to short circuit and from short circuit to forward bias. Stabilised power output (SPO) measurements were undertaken by holding the tested device at a constant voltage around the maximum power point and tracking the power output for 30s or until it reached a constant value, as described in section 2.3. Characterisation of tandem solar cells requires spectral response and external quantum efficiency measurements to ensure both cells are accurately mismatch corrected. Tandem J-V measurements were carried out by collaborators according to published best practice[45].

3.3.2 External quantum efficiency (EQE)

External quantum efficiency measurements were taken in a nitrogen chamber via Fourier transform photocurrent spectroscopy, using the modulated beam of a Bruker Vertex 80v Fourier Transform Interferometer with tungsten lamp source and a Stanford Research SR570 current preamplifier. Samples were calibrated to a Newport-calibrated reference silicon solar cell with a known external quantum efficiency. The solar cells were masked with a 0.0919cm^2 metal aperture to define the active area.

3.4 Optical characterisation

3.4.1 Absorption measurements

Absorption, transmittance and reflectance spectra on thin films were collected in air with a Perkin-Elmer Lambda 1050 UV/Vis/NIR spectrophotometer in transmission mode. Absorption spectra for perovskite precursor solutions were collected in air using a Varian Cary 300 UV-Vis spectrophotometer. Spectra in Fig. 5.5 were taken in vacuum using a Bruker Vertex 80v Fourier-transform infrared (FTIR) spectrometer fitted with a transmission / reflection accessory, a halogen lamp source, and a silicon diode detector.

Tauc plots allow estimation of the optical band gap of a material from absorption spectra. Assuming the absorption coefficient $\alpha(E) = A(E - E_g)^{1/2}$ for a direct band gap material, plotting $(\alpha h\nu)^2$ against energy in eV where ν is frequency is known as a Tauc plot[46]. Reading off the intercept with the energy axis gives an estimate of E_g.

3.4.2 Photoluminescence (PL)

Photoluminescence spectroscopy is a way to probe the recombination dynamics of solar cell materials. Recombination is an essential part of solar cell operation and can either be radiative or non-radiative. Non-radiative recombination usually occurs between an electron in the conduction band and hole in the valence band via a trap state, due to the presence of defects in the material, and is always detrimental to solar cell performance. Radiative radiation is usually band to band, with electrons and holes recombining to produce a photon of energy E_g. Somewhat counterintuitively, radiative recombination is not always detrimental to solar cell performance. High external luminescence is necessary for high solar cell efficiency; light emission actually increases V_{oc}. A solar cell and a light-emitting diode (LED) are reciprocal devices, so it makes sense that a material which makes a good LED with high light emission should also make a good solar cell[47]. Hence good solar cell materials will show high Photoluminescence Quantum Efficiency (PLQE).

Photoluminescence lifetime is the other key performance parameter for recombination in efficient solar cell materials. A material with slow radiative and non-radiative decay rates will have a long excited carrier lifetime, so excited carriers can be collected and produce power in the external circuit before being lost as photons. Some photons produced by radiative recombination can be reabsorbed by the material (photon recycling). This excited carrier lifetime can be extracted by measuring the time-resolved photoluminescence (TRPL), where a short pulse of light generates electron hole pairs which decay over time to lower energy levels of the sample, releasing photons. Fitting the decay rate of excited species over time after a pulsed excitation gives the average carrier lifetime, allowing a measure of the recombination and trap states present in the material.

3.4.3 Steady-state photoluminescence (SSPL)

In SSPL spectroscopy, a semiconductor is excited with a light source that provides energy greater than E_g. The photoexcited carriers then relax down to the band edge and recombine; measuring the wavelength of the radiative emission gives a measure of the band gap energy. For perovskites, the SSPL spectrum is centred at the onset of the absorption spectrum (i.e. very little Stokes shift), which is characteristic for direct band gap semiconductors. Sharp SSPL peaks imply a narrow distribution of states located at the perovskite band edge.

Samples in vacuum were excited using a tunable Ti:Sapphire pulsed (80fs) laser with a wavelength of 800nm and an 80MHz repetition rate (Mai Tai, Spectra-Physics). A BBO crystal was used to double the excitation frequency, giving a wavelength of 400nm. The 800nm fundamental wavelength was filtered out using a polariser and a colour filter. The excitation intensity was attenuated down to 500μW over an area of 0.2mm^2 to give a fluence of approximately 3nJcm^{-2} and vertically polarised. A horizontal polariser and a 550nm long-pass colour filter were placed after the sample to remove any laser scatter from the spectrum. Photoluminescence from the sample was collected by a pair of off-axis parabolic mirrors and focused onto the entry slit of a grating monochromator (Triax, Horiba). The spectrally resolved PL was detected by a nitrogen-cooled Si-CCD detector (Symphony, Horiba) and the spectral response of the detector was corrected for using a tungsten filament lamp with known spectrum. This is particularly important for Sn perovskites since the sensitivity of the CCD drops off in the NIR where these materials emit. SSPL measurements in chapter 6 were carried out in air using a Horiba Scientific Fluorolog spectrofluorometer, with a monochromated xenon light source.

3.4.4 Time-resolved Photoluminescence (TRPL)

Perovskite films were deposited on oxygen plasma treated glass substrates using the same method as the devices. TRPL measurements were taken using a time-correlated single photon counting (TCSPC) setup (FluoTime 300, PicoQuant GmbH). Thin film samples were photoexcited using a 507nm laser head (LDH-P-C-510, PicoQuant GmbH) pulsed at frequencies between 0.3-10MHz, with a pulse duration of 117ps and fluence of ~3μJ/cm2 - 30nJ/cm2. The PL was collected using a high resolution monochromator and hybrid photomultiplier detector assembly (PMA Hybrid 40, PicoQuant GmbH).

3.4.5 Optical-pump/THz-probe spectroscopy (OPTPS)

Perovskite films were deposited on oxygen plasma treated quartz discs using the same method as the devices. The samples in vacuum were photoexcited at 800 nm using the output of an amplified Ti:sapphire laser (1.1kHz, 40fs pulse duration, Spectra Physics, Millennia – Tsunami – Empower – Spitfire), which was filtered with a variable neutral density filter to vary the fluence from 16–151μJ/cm^2. THz probe radiation was generated using optical rectification in a 450μm thick GaP(110) crystal and detected via free-space electro-optic sampling in a ZnTe crystal (0.02mm ZnTe(110) on 3mm ZnTe(110)). To record these time-dependent decay traces, the change in peak THz amplitude (ΔT/T) was measured as a function of the pump-probe delay time. Experimental data was fitted to the rate equation $dn/dt = -k_2n^2 - k_1n$, where n in the charge-carrier density, k_1 is the monomolecular recombination rate, and k_2 is the bimolecular recombination rate constant.

The diffusion length, L_D was calculated at a photoexcitation density of n = 1x10^{15}cm^{-3} using the expression $L_D = \sqrt{D/R_{total}(n)}$. D is the diffusion coefficient with $D = \mu k_B T/q$, where μ is the charge-carrier mobility (taken to equal φμ at room temperature, where excitons are dissociated), k_B is the Boltzmann constant, T is temperature (here 295K), and q is the elementary charge. R_{total} is the total charge-carrier recombination rate given by $R_{total} = nk_2 + k_1$.

3.5 Material characterisation

3.5.1 Scanning electron microscopy (SEM)
Perovskite films were deposited on oxygen plasma treated FTO glass substrates and a Hitachi S-4300 field emission scanning electron microscope was used to acquire SEM images under vacuum.

3.5.2 X-ray diffraction (XRD)
Perovskite films were deposited on oxygen plasma treated FTO glass substrates, followed by a capping layer of polymethyl methacrylate (PMMA), by dynamically spin coating 50μL of a PMMA solution (10mg/ml in chlorobenzene) at 2000rpm for 30s in nitrogen. A PANalytical Empyrean PIXcel^{1D} diffractometer with Cu anode was used to obtain XRD measurements in air. The FTO reference peaks were matched between the diffraction patterns, allowing direct spectral comparison between different samples.

3.5.3 Surface profilometry
In order to measure sample thicknesses, perovskite films were deposited on oxygen plasma treated glass substrates and a small scratch was made with a razor blade to remove the surface of the sample film. A Veeco Dektak 150 surface profilometer was used to measure the thickness between the exposed glass and undisturbed sample film.

3.5.4 Energy-dispersive X-ray spectroscopy (EDX)
Perovskite films were deposited on oxygen plasma treated silicon substrates. EDX measurements were taken using a FEI Quanta 600 FEG scanning electron microscope under vacuum, with an Oxford Instruments INCA Energy detector to determine content of Sn, Pb and F within different areas of the thin films.

3.5.5 Conductivity
Perovskite films were deposited on oxygen plasma treated glass substrates. A 100nm thick gold electrode pattern of a standard four-point probe conductivity design was thermally evaporated directly onto the perovskite films. Conductivity measurements were performed in air using a homemade four-point probe setup, with a force channel length (direction of current flow) of 1mm and a width of 1cm and a sense channel length of 300μm and width of 1mm. The J–V characteristics of these samples were collected at room temperature with a Keithley 2420 source meter unit to extract both the bulk and the contact resistance. The contact resistance was found to be negligible compared to the bulk. Measurements under light were taken with a calibrated AM1.5 solar simulator and a 0.25 sun LED array.

3.5.6 Kelvin probe force microscopy
Perovskite films were deposited on oxygen plasma treated glass substrates. A vibrating Kelvin probe (probe diameter = 2mm, KP Technology, UK) was used to determine the work function. All measurements were done in air. Calibration of the Kelvin probe used a freshly cleaved highly ordered pyrolytic graphite surface which has known work function of 4.65eV[48].

4. Solvent engineering for morphological control and improved performance of formamidinium-based mixed tin-lead perovskite solar cells

4.1 Introduction

To be able to access the theoretical maximum efficiencies for single and multi-junction devices, a range of perovskite band gaps from 1.22 to 2.04eV are required[15]. Direct band gaps around 1.5-1.7eV are accessible using standard lead triiodide perovskites by substituting the A-site with combinations of MA, FA and Cs cations. The band gap can be increased further by substituting the X-site halide anion with bromide[28][31][32]. However, the only route known to lower the band gap below that of $MAPbI_3$ is substitution of the Pb^{2+} cation with Sn^{2+}, with full substitution leading to a perovskite with a 1.4eV band gap. Partial replacement leads to anomalous band gap bending with a minimum band gap at almost 1.2eV at 40-60% lead content[22][35], with a full band gap range of 1.2-1.55eV. These mixed tin-lead perovskites with combinations of MA, FA and Cs have recently been shown to yield efficiencies up to 20%[49], remarkable for materials with large trap densities and short PL lifetimes[20][21][50][51]. These efficient low-band gap perovskites have applications as a replacement for a near-IR absorber for all-perovskite tandem solar cells, with recent reports of monolithic tandem solar cells with efficiencies of up to 24.8%[52].

Fabricating smooth, pinhole-free layers of tin-based perovskite on planar substrates has proved difficult until recently, due to their rapid crystallisation[19]. This chapter details experiments to find a reproducible and reliable deposition method in order to fabricate planar $FASn_xPb_{1-x}I_3$ perovskite thin films for high performance solar cells, and first experiments to produce high performance monolithic and mechanically stacked multi-junction all-perovskite solar cells, with the bottom cell based on Sn-Pb. Most research initially focussed on $MASnI_3$ or $MASn_xPb_{1-x}I_3$ absorber materials; FA-based Sn perovskites have not been studied as much as MA-based Sn perovskites. Because of the advantages of FA in Pb-based perovskites such as improved thermal stability, the initial focus of this chapter is to examine if similar advantages can be gained by using the FA cation within the mixed Sn-Pb system.

4.2 Precursor phase antisolvent immersion

Perovskite thin film fabrication usually proceeds by dissolving precursor salts in a solvent, spin coating this precursor solution onto a substrate, then heating this substrate to remove the solvent, causing supersaturation in the film leading to nucleation and crystallisation. Controlling this crystallisation is important to form heterogeneous nuclei of high density on the substrate, rather than heterogeneous nucleation on colloidal particles and homogeneous nucleation within the precursor solution itself. Following the standard route for Pb-based perovskite preparation, if equimolar amounts of FAI and 50:50 SnI_2:PbI_2 are mixed in dimethylformamide (DMF) and spin coated in a N_2-filled glovebox, $FASn_{0.5}Pb_{0.5}I_3$ perovskite films form almost immediately on the spin coater, but the film quality is poor. To overcome this barrier, two techniques that have been used in the literature in order to control perovskite film crystallisation were combined.

Dimethylsulfoxide (DMSO) is a polar, aprotic solvent which can act as a Lewis base, with a lower vapour pressure and a higher boiling point than DMF. A Lewis base is any species that has a filled orbital containing an electron pair which is not involved in bonding but can donate its lone pair of electrons to a Lewis acid to form a Lewis adduct. SnI_2 and PbI_2 can accept an electron pair and are hence Lewis acids; Sn-based perovskites in DMF crystallise rapidly compared to Pb-based perovskites because SnI_2 is a stronger Lewis acid than PbI_2, so its reaction with MAI or FAI is faster. Previous work has shown that dissolving SnI_2 in DMSO leads to formation of SnI_2•3DMSO complexes, with chemical structure as shown in **Fig. 4.1a**, with the DMSO directly coordinated to the Sn ion[53]. Upon spin coating a solution of FAI and SnI_2 precursors dissolved in DMSO, an intermediate solvated phase of SnI_2•3DMSO is formed on the substrate. This intermediate phase has been shown to be crystalline

from XRD, with the presence of DMSO confirmed by FTIR, with the organic cation remaining dissolved in the solvent. By varying the rate of subsequent DMSO evaporation using heat, perovskite formation can be controlled and heterogeneous nucleation takes place directly on the substrate, a technique that has been demonstrated to be effective for improving the quality of $MASnI_3$ thin films[53].

Use of an appropriate antisolvent to quench and crystallise perovskite films has dramatically enhanced film quality and coverage with Pb-based perovskite systems. Upon application to a wet film, this antisolvent quickly washes off the parent solvent and simultaneously reduces the solubility of the solute. Compared to solvent removal by heating, antisolvent treatment is a very rapid process, suppressing homogeneous nucleation and leading to a smoother and more uniform perovskite film[54]. This antisolvent can either be applied either by gradual dripping onto the perovskite film surface during spin coating[55], or full immersion of the perovskite film into a bath of solvent[56].

Combining these two techniques, rather than using neat DMSO as a solvent, a mixture of DMSO and DMF allowed spin coating of a uniform transparent precursor film. Immersion into an antisolvent bath of anisole (**Fig. 4.1b**) produced an immediate colour change to reddish due to the SnI_2•3DMSO complexes present in the film. These intermediate films are expected to be crystalline as in the published literature; performing XRD analysis of these intermediate compounds is challenging due to their air sensitivity[53]. Subsequent annealing at 70°C removed the residual DMSO, turning the film black. **Fig. 4.1c** shows the colour change of the films during this process. This technique is termed "precursor phase antisolvent immersion"[22]. **Fig 4.1d** shows scanning electron microscope (SEM) images of the different morphologies of $FASnI_3$ films prepared using this technique, with toluene, chlorobenzene and anisole as the quenching antisolvents. Of these, anisole produces the most uniform perovskite films, with a large grain size and few pinholes.

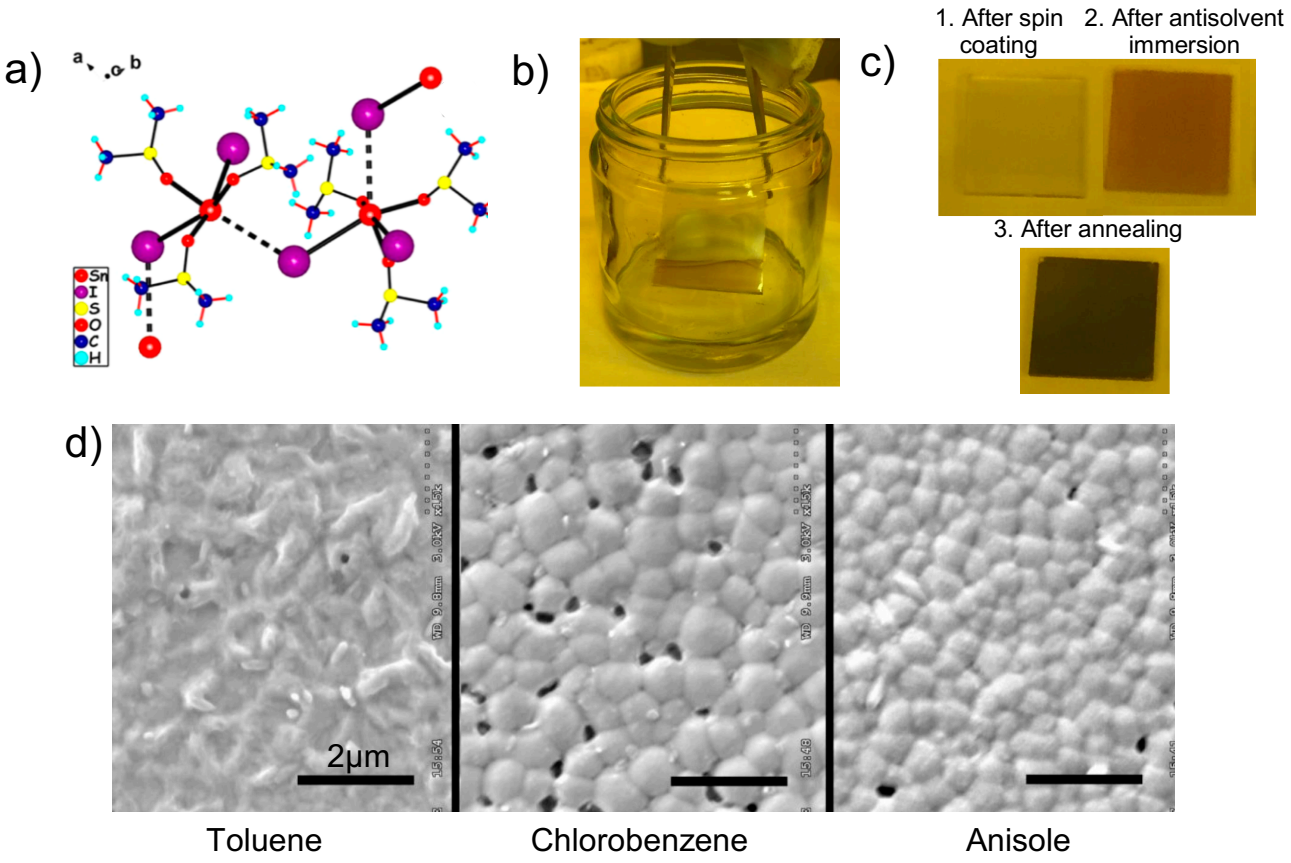


Figure 4.1: a) Crystal structure of SnI_2•3DMSO, an intermediate compound in the perovskite film fabrication process. b) Dipping of perovskite film into antisolvent bath of anisole, showing change from transparent to reddish colour. c) Photographs of $FASn_{0.5}Pb_{0.5}I_3$ films at different stages of the precursor phase antisolvent immersion deposition technique, showing change in colour of the films from colourless to reddish to black. d) Scanning electron microscope (SEM) images showing comparison of different solvents used as the quenching solvent, for $FASnI_3$. Left to right: toluene, chlorobenzene, anisole. The scale bar is 2μm in all cases.

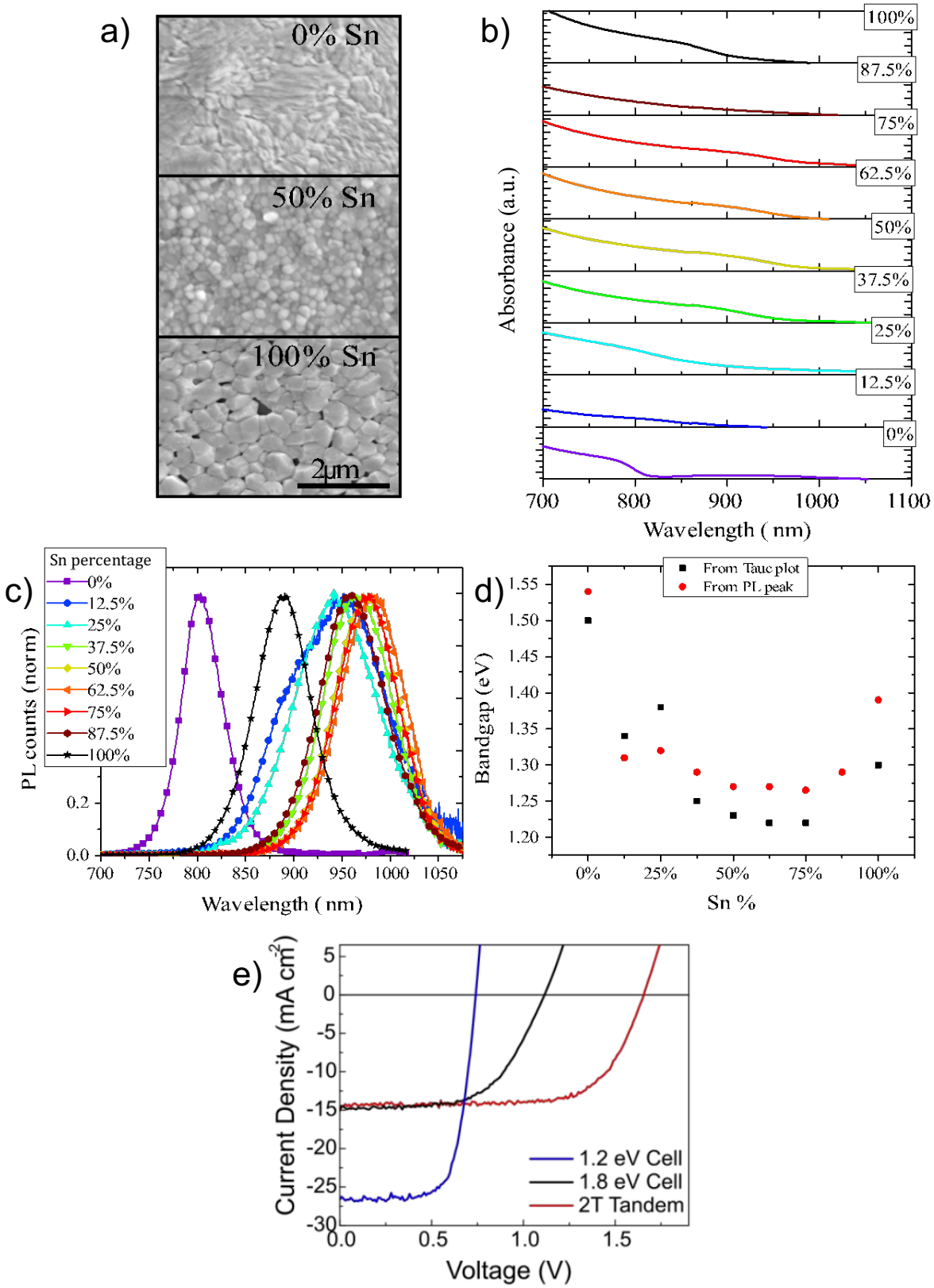


Figure 4.2: a) SEM images showing surface of $FASn_xPb_{1-x}I_3$ thin films with varying percentages of Sn content. b) UV-vis absorption measurements of $FASn_xPb_{1-x}I_3$ films. c) Normalised SSPL spectra of $FASn_xPb_{1-x}I_3$ films. d) Band gap as a function of Sn percentage, determined from the absorption onset in a Tauc plot (assuming direct band gap), and from PL peak position. e) Current density - voltage (J-V) curves for best-performing devices using $FA_{0.75}Cs_{0.25}Sn_{0.5}Pb_{0.5}I_3$ (1.2eV cell), $FA_{0.83}Cs_{0.17}Pb(I_{0.5}Br_{0.5})_3$ (1.8eV cell), and a monolithic 2-terminal all-perovskite tandem device with a 1.2eV cell fabricated directly onto the 1.8eV cell with a sputtered ITO buffer layer in between. Layer thicknesses were optimised in order to reduce optical losses. Reproduced with permission from ref[22]. The thin films presented in (a-d) were fabricated, measured and analysed by G. Eperon. The PV cells presented in (e) were fabricated and measured by T. Leijtens. All films were fabricated by using the precursor-phase antisolvent immersion fabrication method developed in section 4.2.

4.3 $FASn_xPb_{1-x}I_3$ thin film characterisation, single and multi-junction solar cells

Fig. 4.2a, **4.2b**, and **4.2c** show SEM, UV-vis absorption and steady-state photoluminescence (SSPL) measurements on $FASn_xPb_{1-x}I_3$ thin films made using the precursor phase antisolvent immersion method. The SEM images show this method is capable of fabricating uniform smooth, dark, highly crystalline and uniform films over the entire compositional range of 0 to 100% Sn content. **Fig. 4.2d** shows extracted band gaps, from the absorption measurements via the Tauc plot technique, and from the SSPL spectra. The band gap shifts with Sn content from around 1.5eV at 0% Sn, to 1.2eV at 50-75% Sn, then back to 1.3eV at 100% Sn. This anomalous band gap bending is consistent with that seen in the $MASn_xPb_{1-x}I_3$ system[22][35]. No segregation of Sn and Pb in the SSPL spectra is observed, unlike with I and Br in mixed-halide perovskite compositions[33]; these mixed Sn-Pb perovskites are phase stable with the full compositional range from Sn to Pb accessible.

Optical-pump THz probe spectroscopy measurements on $FASn_{0.5}Pb_{0.5}I_3$ perovskites show a diffusion length of around 300nm, equivalent to the typical thickness required to absorb most incident light (300-400nm), and a mobility value of $17 cm^2V^{-1}s^{-1}$, comparable to values for Pb perovskite films[22]. External Quantum Efficiency (EQE) measurements show an absorption edge out to 1020nm, corresponding to the low band gap seen from SSPL and absorption measurements.

Using the antisolvent immersion fabrication method developed above, co-authors at Stanford were able to fabricate planar heterojunction devices in the "inverted" p-i-n architecture comprising ITO / PEDOT:PSS / $FA_{0.75}Cs_{0.25}Sn_{0.5}Pb_{0.5}I_3$ / C_{60} / BCP capped with an Ag or Au electrode. Use of indium doped rather than fluorine doped tin oxide glass (ITO rather than FTO) led to a 0.1V increase in V_{oc}. The substitution of 25% caesium to replace FA had little effect on band gap (remaining at 1.26eV), morphology, crystal structure and charge carrier diffusion lengths, but allowed improvement in short-circuit current density to $26.7 mAcm^{-2}$. The stabilised power output (SPO) of the best performing $FA_{0.75}Cs_{0.25}Sn_{0.5}Pb_{0.5}I_3$ single-junction device was 14.8%. The effects of caesium addition to Sn-Pb perovskites will be discussed further in chapter 6.

In order to examine the suitability of this material in an all-perovskite tandem device, an inverted planar cell based on $FA_{0.83}Cs_{0.17}Pb(I_{0.5}Br_{0.5})_3$ perovskite was fabricated by collaborators at Stanford to use as a wide band gap top cell. This composition has previously been shown to be able to deliver 17% efficient devices with a 1.74eV band gap[34]. Using a sputtered ITO buffer layer and fabricating a low band gap $FA_{0.75}Cs_{0.25}Sn_{0.5}Pb_{0.5}I_3$ cell on top of this device using the antisolvent immersion method developed above, a monolithic 2-terminal all-perovskite tandem with SPO of 17.0% was demonstrated. Using these two solar cells in a mechanically stacked 4-terminal tandem configuration, a maximum SPO of 20.3% was achieved. **Fig. 4.2e** shows current density – voltage (J-V) curves for these best-performing narrow and wide band gap perovskite solar cells, and for the monolithic 2-terminal tandem device.

4.4 Complex-assisted gas quenching

Blowing a stream of N_2 gas onto the perovskite film during spin coating has been shown to be effective as an alternative to antisolvent treatment[57]. The initial wet transparent precursor film is formed on the spin coater and a stream of N_2 is used to drive off the DMF solvent, forming complexes in the same way as the antisolvent method described in section 4.2 prior to thermal annealing. This method, termed "complex-assisted gas quenching", drives the system to a state of supersaturation at a rate quicker than the kinetics of heterogeneous nucleation by heating, thereby preventing the growth of irregular structures that would otherwise result in an uneven film. The technique is antisolvent-free, an advantage which is especially apparent with Sn-based perovskites, which must be fabricated inside an N_2-filled glovebox. An open antisolvent bath can lead to a high solvent atmosphere inside the glovebox, which is difficult to control and may affect reproducibility of experiments.

To compare the difference in photovoltaic performance between perovskite films made with the gas quenching method and antisolvent immersion method, a series of inverted planar heterojunction devices of ITO / PEDOT:PSS / $FASn_{0.5}Pb_{0.5}I_3$ / PCBM / BCP capped with an Au electrode were fabricated. **Fig. 4.3** shows solar cell performance parameters (J_{sc}, V_{oc}, FF, PCE, and SPO) for these devices. In order to determine the optimum fabrication conditions, two different concentrations of SnI_2 / PbI_2 / FAI precursors in the mixed DMF:DMSO solvent, and two different types of FA precursors, one new as supplied and one aged in a glovebox for two weeks, were examined. The best-performing devices were made using 0.75M solutions, a new FA precursor, and gas quenching, with best PCE of 13.7%, SPO of 12.8%, and J_{sc} of 27.7mAcm^{-2}.

In order to deliver a similar boost in short-circuit current density as obtained with the devices in section 4.3, 5% caesium was substituted for FA to make a perovskite with composition $FA_{0.95}Cs_{0.05}Sn_{0.5}Pb_{0.5}I_3$. **Fig. 4.3f** shows a current density - voltage (J-V) curve for the best-performing device of this composition, with PCE of 14.1%, SPO of 13.6% and a high J_{sc} value of 29.3mAcm^{-2}. This high performance shows that the gas quenching method can produce Sn-Pb perovskite films of comparable quality, and solar cells of similar performance to the antisolvent immersion technique.

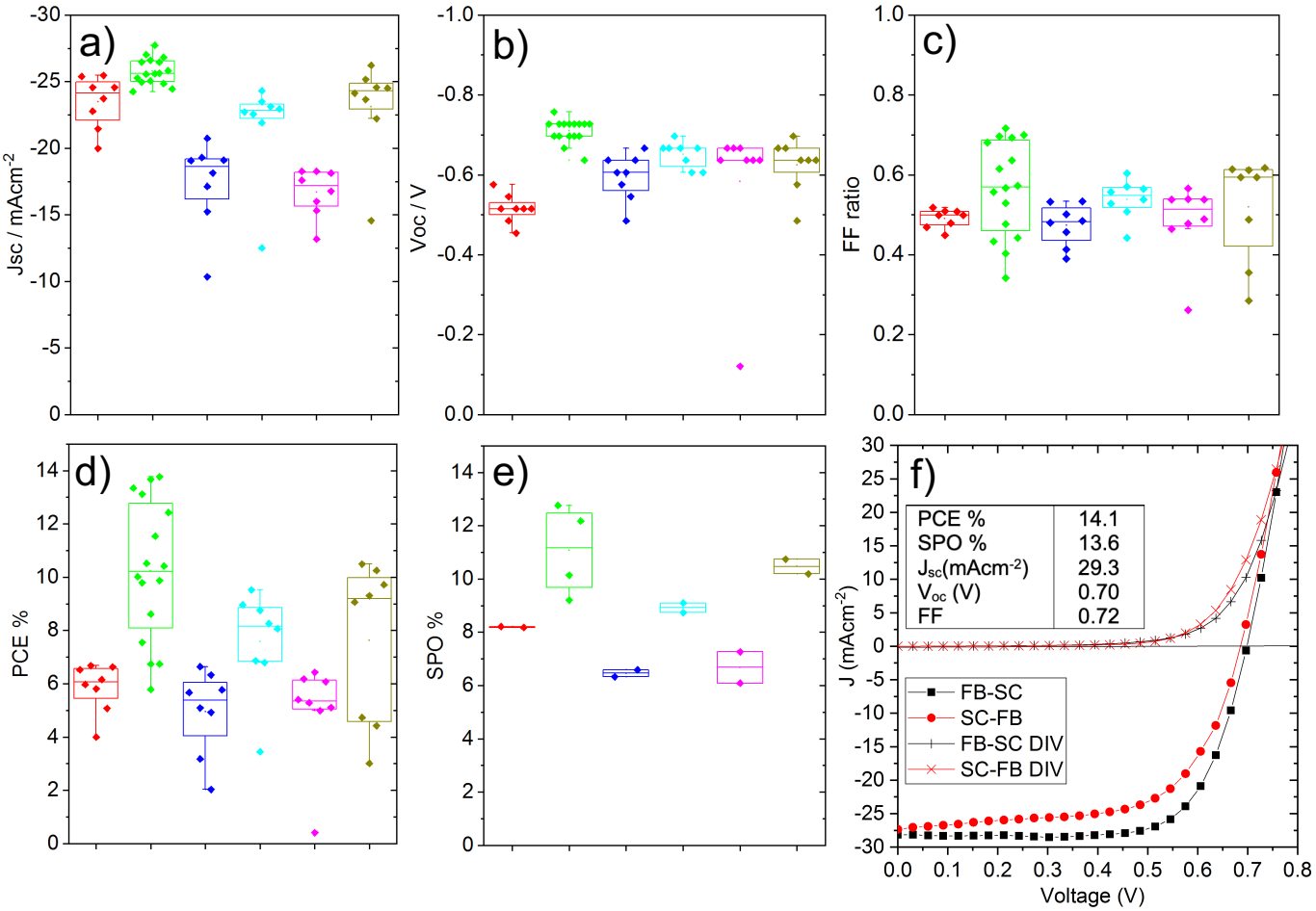


Figure 4.3: Solar cell performance parameters a) short-circuit current density (J_{sc}), b) open-circuit voltage (V_{oc}), c) fill factor (FF), d) power conversion efficiency (PCE), and e) stabilised power output (SPO), for devices made using $FASn_{0.5}Pb_{0.5}I_3$ perovskite, with different solute concentrations in mixed DMF:DMSO solvent, different FA precursors, and fabrication using an antisolvent immersion or gas quenching technique. From left to right: 0.75M solutions, new FA precursor, anisole/gas. 1M solutions, new FA precursor, anisole/gas. 1M solutions, FA precursor aged in glovebox, anisole/gas. f) Current density - voltage (J-V) curves and performance parameters for best-performing device using $FA_{0.95}Cs_{0.05}Sn_{0.5}Pb_{0.5}I_3$ perovskite, from forward bias to short circuit (FB-SC), short circuit to forward bias (SC-FB) and J-V curves in the dark (DIV) for the same device.

4.5 Correlating optoelectronic defectiveness across the full range of (Sn:Pb) content[58]

The accessibility of the full range of band gaps in the FA-based Sn-Pb perovskite system together with the universal gas quenching deposition protocol means that these perovskites could be highly applicable in multi-junction perovskite solar cell applications requiring precisely tuned band gaps. In order to investigate how Sn impacts optoelectronic quality and identify any sources of defectiveness, here the $FA_{0.83}Cs_{0.17}Sn_xPb_{1-x}I_3$ family of materials were examined, paying special attention to low Sn percentages, replacing between 0.001% and 70% of the Pb content. 17% Cs was substituted at the A-site for FA because this composition has been proven to yield a crystallographically and thermally stable three-dimensional triiodide perovskite phase with neat Pb[34].

To probe the charge transport properties of each composition at a length scale relevant to devices, lateral conductivity measurements were performed using a four-point probe setup under both illuminated and dark conditions. **Fig. 4.4** shows the perovskite film conductivity in the dark is initially very low when the Sn fraction is below 20%, with a monotonic increase with Sn content thereafter. This conductivity rise is consistent with sub-band gap absorption and p-doping due to a rise in Sn^{2+} vacancies with Sn content: it has been proposed that the formation energy of Sn^{2+} vacancies is low in neat Sn materials, but increases in mixed Sn-Pb perovskites as the presence of Pb^{2+} in neighbouring lattice B-sites raises the energy required to break metal-halide-metal bonds[59]. Therefore as Sn content increases in the films, more vacancies are likely to be created, leading to p-doping. The p-doping of Sn-Pb perovskites and Sn^{2+} vacancies will be discussed in more detail in chapter 5.

Under illumination, the conductivity of the pure lead perovskite is several orders of magnitude higher than in the dark as photoexcited carriers are now able to conduct and carry charge. On Sn addition, measured film conductivities do not monotonically increase, but begin to drop at 0.5% and pass through a local minimum at 5% that is several orders of magnitude lower than the initial value, before increasing exponentially. This anomalous reduction in light conductivity begins at 0.5% Sn and returns to the initial value of 10^{-4} Scm^{-1} around 30% Sn; in this region there is a significant decrease in solar cell performance, and PL lifetime and PLQE drop by an order of magnitude[58]. This behaviour suggests that Sn introduces trap states in the 0.5%-20% compositional range, through which trap-assisted recombination dominates over the competing mechanism of hole doping to reduce charge carrier transport. As there are no selective contacts in the conductivity measurements, non-radiative recombination can be attributed to the presence of traps within the perovskite thin film itself.

This suggests that band gaps between 1.35 and 1.5eV are unlikely to be useful for optoelectronic applications without developing countermeasures to improve material quality. Likewise, unintentional contamination by Sn is unlikely to impact the photovoltaic performance of neat Pb perovskites since they are tolerant up to about 0.1% Sn content. However, highly efficient narrower band gap materials such as those with 50% Sn content as described in 4.2 and 4.3 above are possible below 1.33eV and are suitable for the bottom cell in tandem perovskite photovoltaics.

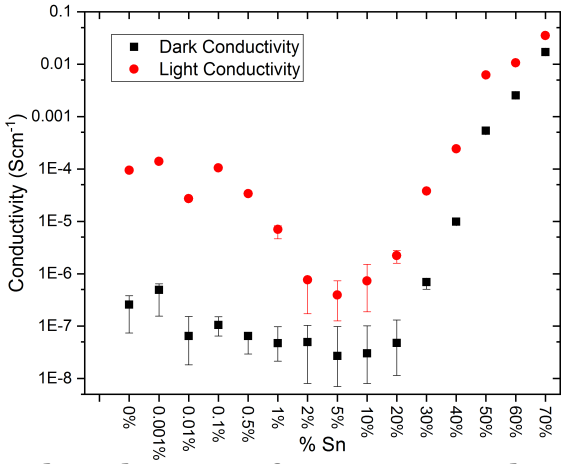


Figure 4.4: Long-range lateral conductivity of $FA_{0.83}Cs_{0.17}Sn_xPb_{1-x}I_3$ perovskites measured with a four-point probe setup (1mm channel length) in the dark and under illumination with a 0.25 sun LED array. The thin films were fabricated by M. Klug.

4.6 Conclusion

Combining two techniques from the literature for fabricating high quality perovskite films, a precursor phase antisolvent immersion technique was demonstrated to overcome the rapid crystallisation of Sn-based perovskites, by using a mixed solvent of DMF:DMSO together with an appropriate antisolvent. This allowed the fabrication of pinhole-free (FA:Cs)(Sn:Pb)I_3 thin films with low band gap, long diffusion length and high mobility. The antisolvent in this method can be replaced with a stream of N_2 without detrimental effects on film quality; this is termed the complex-assisted gas quenching method. Use of these methods to make thin films based on the FA cation resulted in much improved single-junction solar cell performance compared to previous results using MA-based Sn-Pb perovskites.

Changing the Sn content from 0 to 100% showed anomalous band gap bending, with a minimum around 1.2eV for 40-60% Sn. These high performance mixed Sn-Pb perovskites are highly appropriate for all-perovskite multijunction photovoltaic modules, and efficient 2-terminal and 4-terminal all-perovskite tandem devices were demonstrated using these materials. A region of optoelectronic defectiveness was identified between 0.5-20% Sn content, corresponding to band gaps between 1.35 and 1.5eV, suggesting that in this region Sn is introducing sub-band gap trap states into the material.

5. The role of additives as reducing agents and tin vacancy compensators in low band gap perovskite solar cells

5.1 Introduction

The instability of tin in its Sn^{2+} state and ready oxidation to Sn^{4+} is a major concern in development of mixed tin-lead perovskites. However, the mechanism for this oxidation and whether it occurs in precursors, in solutions, in thin films, or in devices, is not clear. Many sources state that spontaneous hole doping caused by oxidation of Sn^{2+} to Sn^{4+} makes the materials more metallic, but this oxidation should theoretically n-dope the material rather than p-dope it[60]. Instead, the large background hole density is likely to be caused by Sn^{2+} vacancies rather than by the presence of Sn^{4+} in the crystal lattice. From density functional theory (DFT) calculations, these vacancies have a low formation energy on creation of the crystal, leaving a gap in the lattice that would otherwise be filled by a 2+ ion. To resolve this apparent violation of charge neutrality, two holes will be released from the valence band to compensate for each Sn^{2+} vacancy, and the energy level of the vacancies is such that the holes are not trapped but induce p-doping in the perovskite[61][58]. The tin vacancy is a shallow acceptor state near the valence band edge. This has been shown to create a monomolecular radiative recombination pathway 3 orders of magnitude higher than for Pb perovskites, which limits electron mobility, the limiting factor for charge transport as hole mobility is high.[21] No photon recycling is possible from this radiative recombination pathway because emitted photons are too low in energy to be re-absorbed by the crystal lattice. This limiting electron mobility for Sn based perovskites could also provide an explanation why the best-performing pure-Sn devices took several years to surpass efficiency records set in 2014[19]. These devices based on a meso-superstructured architecture worked well with good open-circuit voltage (V_{oc}) because electrons had only a short distance to travel to get to the mesoporous TiO_2 scaffold. Due to the large underlying hole density, hole extraction is still straightforward, even though holes must travel relatively further.

Tin(II) fluoride, SnF_2, has been added to tin-based perovskites since 2012 [16][62] and has been shown to enhance performance. SnF_2 has been suggested to suppress the oxidation of Sn^{2+} in order to reduce Sn^{2+} vacancies. Seok and co-workers have fabricated $FASnI_3$ films using a SnF_2-pyrazine complex[63], and Kanatzidis et al have use hydrazine as a reducing solvent atmosphere to suppress vacancies[64] and subsequently added SnI_2 to further enhance this[65]. Recently, addition of SnF_2 has also proved crucial when using an evaporation method to produce perovskite films[66]. However, a detailed understanding of the influence of SnF_2 remains unclear. Most current studies on SnF_2 addition only examine low-performing <8% efficient pure Sn materials, and a study of the importance of additives in high performing Sn-Pb solar cells has not been undertaken. Addition of Pb has been shown to have a stabilising effect, hence it is especially important to investigate the necessity of the SnF_2 additive for these mixed-metal devices[22].

This chapter aims to present a systematic study of the role of SnF_2 in solutions, films and solar cells of mixed Sn-Pb perovskites, discover the mechanism for the improvement in performance caused by addition of SnF_2, and investigate other additives which may have a similar function, namely tin(II) chloride, $SnCl_2$. An inverted structure (ITO/PEDOT/perovskite/PCBM/BCP/Ag) is used for solar cells, as lithium or cobalt salts present in a Spiro-OMeTAD hole transporting material can damage the Sn-based perovskite films[19]. This also minimises hysteresis effects caused by the architecture.

The perovskite $FAPb_{0.5}Sn_{0.5}I_3$ is chosen as an example high performance low-band gap system which does not have the additional complexities of multi-cation combinations. The additives chosen are SnF_2 and $SnCl_2$, as it is possible that Br from $SnBr_2$ could incorporate into the lattice, whereas the F^- and Cl^- anions are too small. A mixed low vapor pressure solvent, dimethylformamide: dimethylsulfoxide (DMF:DMSO) together with a complex-assisted gas quenching technique[57] is used to form the perovskite films, as described in the previous chapter.

5.2 Effect on solutions

Solutions were prepared by dissolving SnI_2, PbI_2 and FAI precursors in a mixture of DMF:DMSO (65:35). **Fig. 5.1a** shows photos of a newly prepared $FASnI_3$ solution where no precursors have knowingly been exposed to air, and the same solution on addition of SnF_2, showing an initial orange colour that changes to yellow on SnF_2 addition. **Fig. 5.1b** shows photos of $FAPb_{0.5}Sn_{0.5}I_3$ solutions with different amounts of SnF_2 and $SnCl_2$ additives after being removed from an N_2 atmosphere to air. A colour change is observed from yellow-orange-red, and the timescale of this change depends on the amount of additive present in the solution, from 5 minutes with no additive, to over 60 minutes for a 40% molar excess of SnF_2 or $SnCl_2$. The speed of this change is independent of moisture, suggesting a reaction is occurring with oxygen rather than water. When present in solution, SnF_2 and $SnCl_2$ slow this colour change on exposure to air at a similar rate, while SnI_2 has no effect. Pure $FASnI_3$ solution changes colour faster than $FAPb_{0.5}Sn_{0.5}I_3$, possibly due to different degradation pathways and stabilisation of Sn when Pb is substituted; it is interesting to note this stabilisation occurs in solutions as well as thin films, which would not be explained by an octahedral sharing hypothesis[59]. **Fig 5.1c** shows ultraviolet–visible spectroscopy measurements on solutions of $FASnI_3$. Over time in air, maxima can be seen emerging at 365nm and 295nm, matching theoretical and measured values for I_3^-[67]. When SnF_2 was added to air-degraded solution, these maxima disappear.

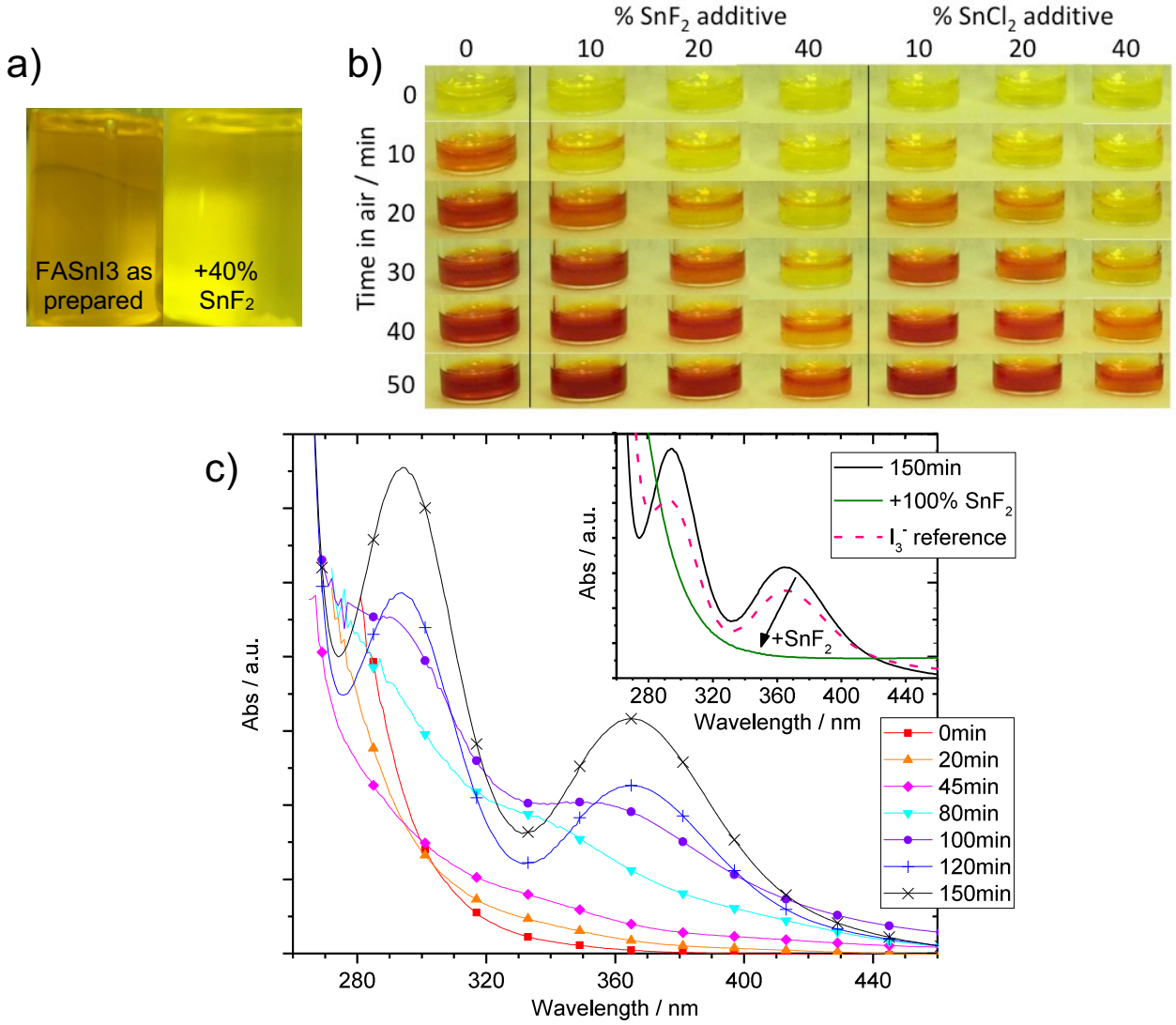


Figure 5.1: a) Photographs of $FASnI_3$ solution as prepared, and on addition of SnF_2. b) Photographs of $FAPb_{0.5}Sn_{0.5}I_3$ solution degrading in air over 50 minutes, with different % molar excess of SnF_2 or $SnCl_2$ additives present in solution. c) Ultraviolet-visible spectroscopy of $FASnI_3$ solution degrading in air. Inset: addition of 100% SnF_2 to solution after 150 min degradation, and reference spectra for I_3^-.

SnF_2 and $SnCl_2$ are both reducing agents; the standard redox potential, E_0, of Sn^{2+}/Sn^{4+} = +0.15 V, compared to the Pb^{2+}/Pb^{4+} system with E_0 = +1.67 V. Additives with Sn^{2+} ions present (SnF_2, $SnCl_2$) will add more Sn^{2+} ions to the solution in total, and any reduction of pre-existing $Sn^{4+} \rightarrow Sn^{2+}$ will be coupled with oxidation of added $Sn^{2+} \rightarrow Sn^{4+}$. Hence on additive addition (before any reactions in solution occur), the amount of Sn^{2+} will be increased, and the overall amount of Sn^{4+} will remain the same. The orange colour of newly prepared $FASnI_3$ solution has previously been attributed to Sn^{4+} ions[68], however this cannot be the case, as on additive addition the concentration of Sn^{4+} should stay approximately constant, so no colour change to yellow should be observed. Instead, the UV vis measurements show this colour is likely to be due to I_3^- arising from the end products of the degradation, which is reduced to I^- on addition of Sn^{2+}, causing the orange colour to disappear.

In order to make a high quality AMX_3 perovskite film, the stoichiometry of the solution has to be precisely balanced. If precursors such as SnI_2 contain some already degraded Sn^{4+} (demonstrated by the presence of I_3^- ions in $FASnI_3$ solution with no air exposure), incorrect weighing of the precursor could occur, leaving the solution deficient in Sn, both 2+ and 4+. Adding SnF_2 or $SnCl_2$ restores the stoichiometric balance of metal:organic cations by adding excess Sn^{2+}, allowing the formation of a Sn(II) based perovskite film without additional pinholes resulting from Sn^{2+} vacancies. Additionally, the balance of I^- ions will be restored as I_3^- is reduced (even though additional Sn^{4+} will be produced, Sn^{2+} will still be in excess). This implies that SnF_2 and $SnCl_2$ can have a dual role as Sn^{2+} compensators and I_3^- reducing agents in precursor solutions.

5.3 Effect on thin films: SEM, EDX, XRD

In order to investigate the role of these additives in crystalline perovskite, thin films of $FAPb_{0.5}Sn_{0.5}I_3$ were produced by a gas quenching method from precursor solutions containing different molar excesses of SnF_2[57]. On additive addition, slower crystallisation during spin coating was observed; with no SnF_2 the films turned red during spin coating even without any gas quenching, and with increasing amounts of additive the films took longer to change colour under the gas stream (a similar effect was seen with a solvent quenching rather than a gas quenching method[22]). **Fig. 5.2a** shows SEM images of $FAPb_{0.5}Sn_{0.5}I_3$ films with varying amounts of SnF_2. With no additive some pinholes can be seen. When SnF_2 is added to these solutions, the morphology improves with a larger grain sizes, with average size increasing from 160nm with no additive to 230nm with 5% SnF_2. From surface profilometry measurements, addition of SnF_2 leads to an increase in film thickness from 280-300nm with no additive, to 300-350nm with 2.5% SnF_2.

In films with more than 20% molar excess SnF_2, a secondary "shard" phase is observed. At what molar excess this phase begins to occur is not always reproducible between batches of films. This irreproducibility could be due to oxidation either at the precursor or solution stage; the more oxidation that has already occurred, the more SnF_2 is required to re-balance the stoichiometry and hence the secondary phase will appear at higher molar excesses of SnF_2. As more SnF_2 is added, more secondary phase shards appear on the film until pinholes begin to form again at 75% excess SnF_2. **Fig. 5.2b** shows SEM images of films with $SnCl_2$ addition; a similar improvement in morphology from films with no additive can be seen, but with a secondary phase appearing at lower molar excesses of $SnCl_2$ than it did with SnF_2, and large pinholes appearing with 40% excess $SnCl_2$.

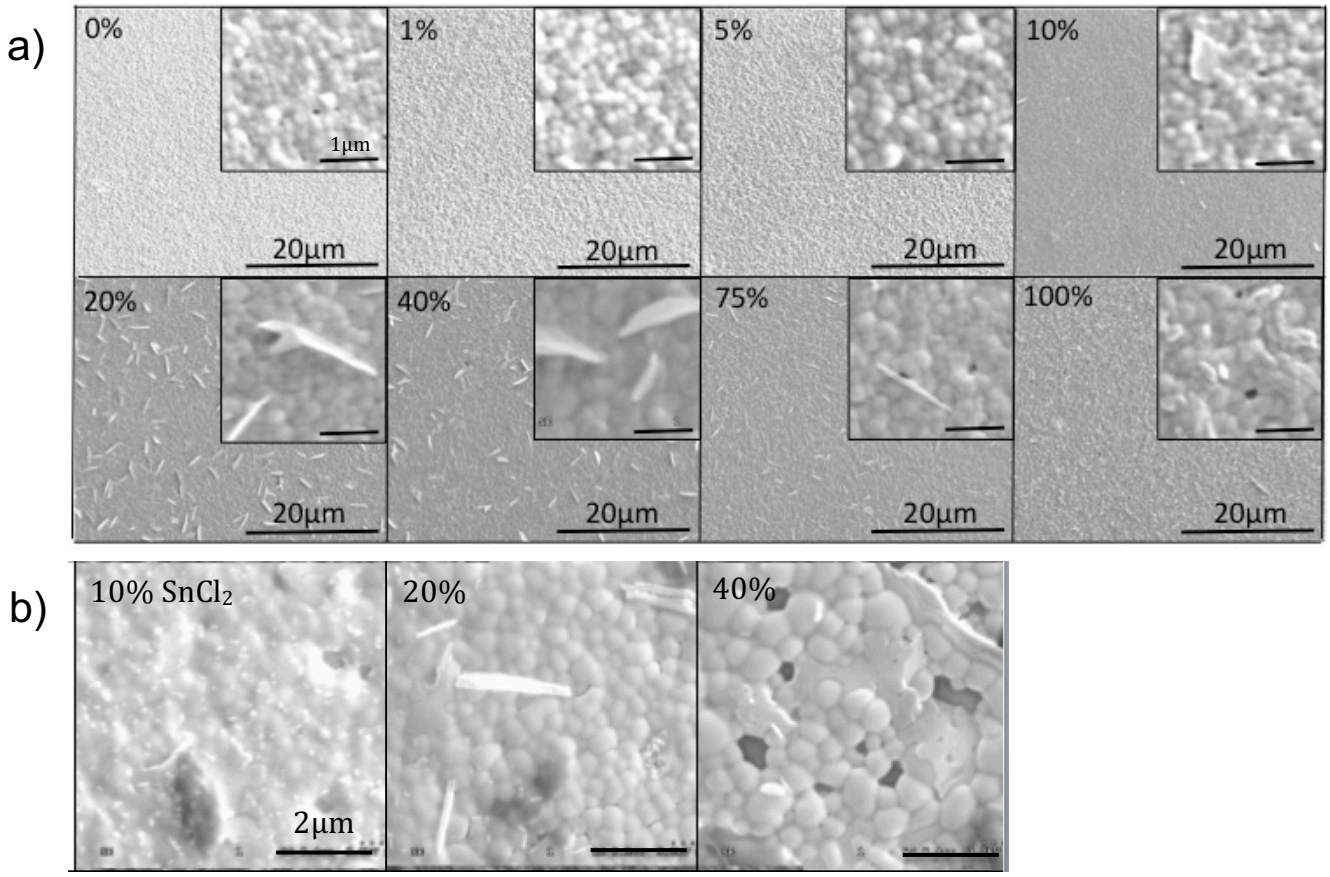


Figure 5.2: a) Scanning electron microscopy (SEM) images of $FAPb_{0.5}Sn_{0.5}I_3$ films on FTO glass prepared with different molar excesses of SnF_2. The scale bar on the inset images is 1µm. b) SEM images of $FAPb_{0.5}Sn_{0.5}I_3$ films on FTO glass prepared with different molar excesses of $SnCl_2$. The scale bar is 2µm.

In order to classify these secondary phase shards, Energy-dispersive X-ray spectroscopy (EDX) and X-ray diffraction (XRD) measurements were performed. **Fig. 5.3a** shows the ratio of Sn ions compared to Pb ions present in $FAPb_{0.5}Sn_{0.5}I_3$ films determined using EDX, in two different regions of the film: the bulk grains, and the secondary phase shards that can be seen at higher SnF_2 concentrations. It is usual practice to write the chemical formula of perovskite films according to the ratio of precursors added into solution; for example the perovskite tested here is described as $FAPb_{0.5}Sn_{0.5}I_3$ because a solution containing equal amounts of SnI_2 and PbI_2 is used, however the true ionic ratios present in the lattice may be different from this. To the best of the author's knowledge, this is the first time these ionic ratios have been directly tested for mixed Sn-Pb perovskites. For the sample with no additives, the Sn:Pb ratio is 0.8-0.9 (Sn deficient), the ratio at 20% SnF_2 is almost 1:1 and at 40% is 1.2-1.3. With no additives, about 10-20% of the Sn^{2+} presumed to be in the solutions is not present in the lattice – this could have already been oxidised to Sn^{4+} either in the precursor solutions or during film formation. Adding the right amount of SnF_2 restores the Sn:Pb ratio to the expected stoichiometric value.

Examining the secondary phase shards in EDX shows they are Sn-rich, with 2-3x as much Sn as the bulk material, and the ratio of excess Sn:F is close to 2. This would suggest the secondary phase is SnF_2 and not SnF_4 or SnO_2. **Fig. 5.3b** shows the XRD pattern of $FAPb_{0.5}Sn_{0.5}I_3$ films with no additive and with 40% SnF_2, compared with the XRD patterns of SnF_2 and SnF_4 powders. In the 40% SnF_2 sample a peak at 26.2° can be seen which corresponds with the SnF_2 powder XRD, also implying the secondary phase shards are likely to be SnF_2 and backing up the EDX result. However, SnF_4 could still be present in the films, as it has a very weak powder XRD pattern. The bulk XRD pattern is relatively unchanged, showing that no fluoride ions have been incorporated into the lattice, which is expected due to its small ionic size compared to bromide or iodide. It is unlikely Cl is incorporated on $SnCl_2$ addition for the same reasons. On addition of SnF_2 the 110 and 220 peaks increase in intensity, which could be due to a different preferred crystal orientation in films with SnF_2.

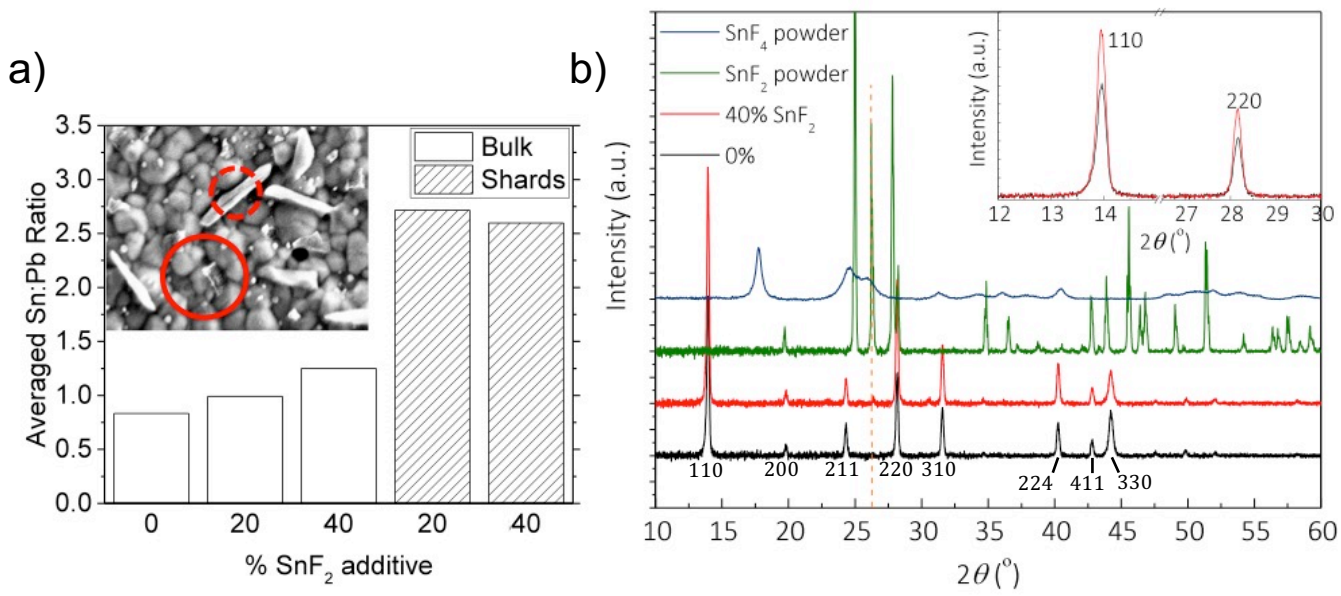


Figure 5.3: a) Averaged Sn:Pb ratio from calculated from energy-dispersive X-ray spectroscopy measurements on $FAPb_{0.5}Sn_{0.5}I_3$ samples with different molar excesses of SnF_2, taken at two different points in the samples: the bulk and the shards, as shown in the inset SEM image. b) X ray diffraction (XRD) pattern of $FAPb_{0.5}Sn_{0.5}I_3$ samples prepared without additives and with a 40% molar excess of SnF_2, plotted alongside powder XRD patterns of SnF_2 and SnF_4. Inset: magnified view of the region from 2θ values of 12-15 and 27-30, showing the 110 and 220 peaks of $FAPb_{0.5}Sn_{0.5}I_3$. The thin films presented in (b) were measured by Z. Wang.

5.4 Effect on Solar Cell parameters

To examine the photovoltaic performance of these thin films, a series of planar heterojunction devices in the "inverted" p-i-n architecture comprising ITO / PEDOT:PSS / $FAPb_{0.5}Sn_{0.5}I_3$ / PCBM / BCP capped with an Au electrode were fabricated. The current density - voltage (J-V) curves and stabilised power output (SPO) at various SnF_2 and $SnCl_2$ additive concentrations for best-performing devices are shown in **Fig. 5.4**.

With no additives, solar cells show poor reproducibility, both within a single batch and between batches. With additives, the SPO is improved and hysteresis is significantly reduced, and the open-circuit voltage V_{oc} improves dramatically as the morphology improves, probably due to the lower number of pinholes in the film, reducing the leakage current. As more additives are introduced, the secondary phase starts to appear, causing a rougher film, which could lead to shunting as the shards poke through the PCBM, hence causing a decrease again in V_{oc}.

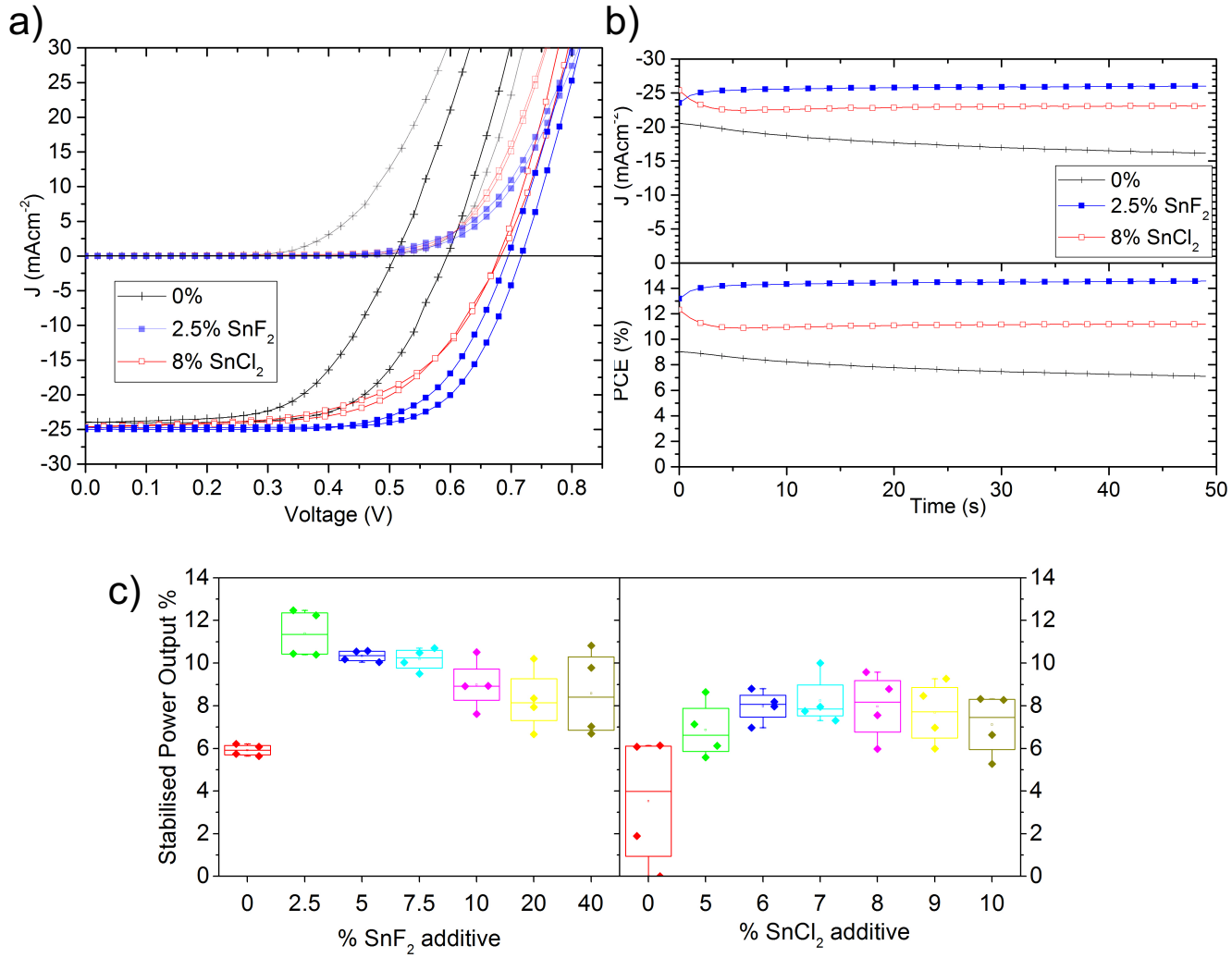


Figure 5.4: a) Current density - voltage (J-V) curves for best-performing devices using $FAPb_{0.5}Sn_{0.5}I_3$ perovskite with no additive, with SnF_2 additive and with $SnCl_2$ additive. b) Stabilised power output (SPO) for best-performing devices with no additive, with SnF_2 additive and with $SnCl_2$ additive. c) SPO for best-performing devices at different molar excesses of SnF_2 and $SnCl_2$ additives.

	0%	2.5 % SnF_2	8% $SnCl_2$
PCE %	9.2 ± 2.5	12.7 ± 0.7	10.3 ± 0.5
SPO %	6.1 ± 0.5	12.5 ± 0.2	9.6 ± 0.4
J_{sc}($mAcm^{-2}$)	23.9 ± 5.0	24.8 ± 1.5	24.6 ± 1.0
V_{oc} (V)	0.60 ± 0.01	0.72 ± 0.01	0.70 ± 0.01
FF	0.65 ± 0.05	0.71 ± 0.01	0.59 ± 0.05

Table 5.1: Power conversion efficiency (PCE), stabilised power output (SPO), short-circuit current density (J_{sc}), open-circuit voltage (V_{oc}) and fill factor (FF), for best-performing solar cells with no additive, with SnF_2 additive and with $SnCl_2$ additive. Uncertainties are calculated from the standard deviation of device performance parameters within a batch.

Table 5.1 shows solar cell performance parameters for champion devices with different additives. The optimum concentration of SnF_2 for highest efficiency solar cells (champion SPO 12.5%) was found to be only 2.5% molar excess, smaller than the 10-20% standard in much of the literature, a value that has been carried over from research on pure Sn devices[22][50]. The lower optimum additive concentration in mixed Sn-Pb perovskites implies that the addition of lead does add some stabilisation to the thin films[59]. The optimum concentration of SnF_2 varies between batches, due to variations in the degree of initial oxidation of the precursors, solutions, and the atmosphere in the N_2 filled glovebox during fabrication. There is only a 3% drop in SPO between 2.5% and 40% SnF_2 excess, showing the perovskite film can tolerate large amounts of SnF_2 while maintaining high performance.

A similar trend is observed on $SnCl_2$ addition, with greatly improved device reproducibility and a maximum V_{oc}, short-circuit current density J_{sc} and power conversion efficiency PCE at 8% $SnCl_2$. The best SPO of 9.6% is lower than that with an SnF_2 additive. The performance parameters are also much more sensitive to the exact concentration of $SnCl_2$ than using SnF_2, with just a small % increase or decrease in $SnCl_2$ excess having a large effect. This more sensitive dependence coupled with the batch-to-batch variation of optimum additive concentration means it is hard to predict the right amount of $SnCl_2$ to guarantee high performing devices. The ability of the films to tolerate large variations in SnF_2 content implies it is a better choice of additive than $SnCl_2$.

5.5 Trap reduction in films: EQE, THz, TRPL

Table 5.2 shows optical-pump THz probe spectroscopy measurements on samples of $FAPb_{0.5}Sn_{0.5}I_3$ prepared with no additives, and molar excesses of SnF_2 and $SnCl_2$. **Fig. 5.5a** shows steady-state photoluminescence (SSPL) and **Fig. 5.5b** shows time-resolved photoluminescence (TRPL) measurements of samples prepared with no additives and different amounts of SnF_2. On addition of 20% SnF_2, TRPL lifetimes increase from 0.5ns to 1.4ns, mobilities increase from $8cm^2V^{-1}s^{-1}$ to $12cm^2V^{-1}s^{-1}$ and diffusion lengths from 75nm to 166nm. Films with 8% $SnCl_2$ show mobilities improved to $11cm^2V^{-1}s^{-1}$ and diffusion lengths of 183nm. SnF_2 does not affect SSPL peak position or linewidth, even in a sample with a very large 100% SnF_2 excess. UV-vis absorption Spectra (**Fig. 5.5c**) also show that the absorption onset is not changing, implying the perovskite band gap is not changing much with SnF_2 addition, despite the Sn:Pb ratio having been shown to be changing from 40-60% Sn content from the EDX measurements. Previous measurements have shown there is a plateau in band gap around 50% Sn, but at other starting ratios of Sn:Pb the perovskite band gap could also be affected by additive addition[22].

Sample	μ ($cm^2V^{-1}s^{-1}$)	k_1 (s^{-1})	k_2 (cm^3s^{-1})	L_D (nm)
No additive	8 ± 2	(3.4 ± 0.1) $\times 10^9$	(4.8 ± 0.2) $\times 10^{-10}$	75 ± 9
20% SnF_2	12 ± 2	(1.0 ± 0.1) $\times 10^9$	(3.0 ± 0.2) $\times 10^{-10}$	166 ± 16
8% $SnCl_2$	11 ± 2	(0.8 ± 0.1) $\times 10^9$	(2.9 ± 0.2) $\times 10^{-10}$	183 ± 20

Table 5.2: Short-range short-time charge-carrier mobility μ, monomolecular recombination constant k_1, bimolecular charge-carrier recombination rate constant k_2, and charge-carrier diffusion length L_D for $FASn_{0.5}Pb_{0.5}I_3$ thin films, determined from optical-pump/THz-probe spectroscopy (OPTPS). The thin films were measured by R. Milot.

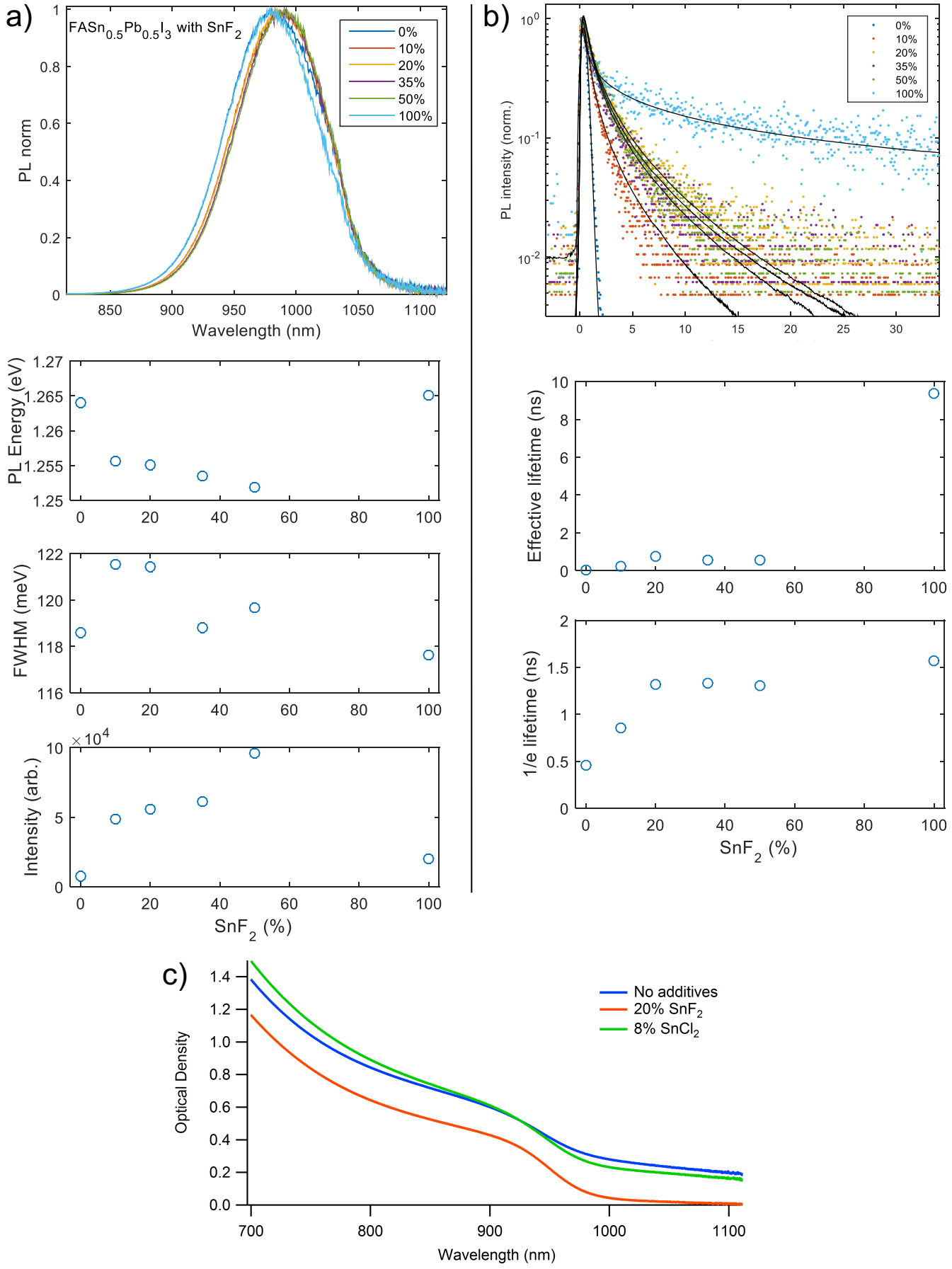


Figure 5.5: a) Normalised steady-state photoluminescence (SSPL) spectra of $FAPb_{0.5}Sn_{0.5}I_3$ thin films prepared with different SnF_2 molar excesses, extracted peak PL energy, full width at half maximum (FWHM) and peak intensity. b) Time-resolved photoluminescence (TRPL) measurements of the same films, extracted effective and 1/e lifetimes. c) UV-vis absorption spectra of $FASn_{0.5}Pb_{0.5}I_3$ thin films with and without SnF_2 and $SnCl_2$ additives. UV-vis absorption offsets between samples are due to different film thicknesses. The thin films presented in (a-b) were measured by E. Parrott. The thin films presented in (c) were measured by R. Milot.

Fig. 5.6a shows the External Quantum Efficiency (EQE) of devices prepared with 5% molar excess SnF_2 and without additives. There is a significant spectral change in the region 400-650nm with substantially enhanced EQE in devices made with SnF_2 additive. The EQE is low in the range 700-900nm, probably due to the relatively thin films (300nm). Interference effects can also be seen across the rest of the spectrum. Recent device improvements have allowed the use of thicker films by improving the minority carrier diffusion length using combinations of cations[69].

The increased TRPL lifetime and higher mobility on additive addition suggest that by adding SnF_2, the fabricated perovskite film contains fewer defects that could act as traps and recombination centres. If the SnF_2 is eliminating some shallow traps such as Sn^{2+} vacancies and the sample ends up less doped, the electron recombination rate with dopant holes is reduced which gives the longer electron diffusion lengths seen from THz spectroscopy (Table 5.2). For shorter wavelength photons, the originally created charge-carrier density profile is more uneven through the film depth than for longer wavelength photons. A longer electron diffusion length will therefore have a bigger effect on the prospects of electrons generated from shorter wavelength photons than on electrons generated from longer wavelength photons, since electrons from shorter wavelength photons are on average generated nearer the PEDOT and have further to travel to the PCBM. This will therefore lead to increased charge collection from shorter wavelength photons in films with SnF_2, explaining the substantially enhanced EQE in that region. **Fig. 5.6b** shows a schematic of this process.

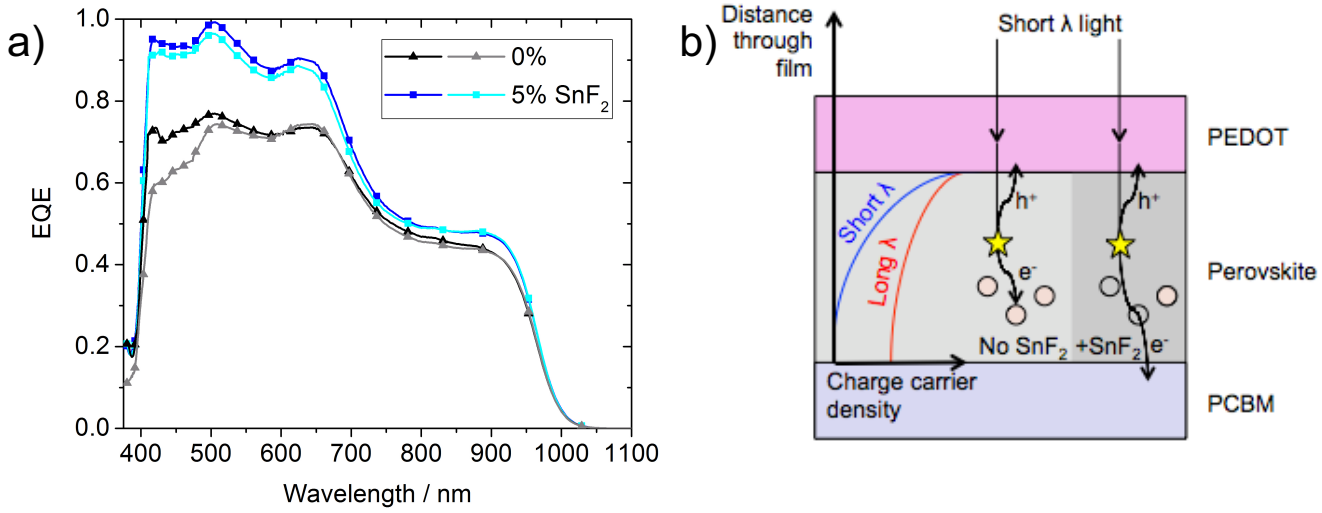


Figure 5.6: a) External Quantum Efficiency (EQE) measurements of four devices, two prepared without additives and two with 5% SnF_2. b) Proposed mechanism for enhanced EQE in shorter wavelength regions with SnF_2 additive: charge-carrier density profiles for photons of different wavelengths; perovskite with no additives showing electrons generated from short wavelength photons close to the PEDOT interface unable to reach the PCBM due to Sn^{2+} vacancy traps; the same perovskite with SnF_2 additive showing more of these short wavelength generated electrons now able to reach the PCBM, due to eliminated trap states and hence a longer electron diffusion length. The thin films presented in (a) were measured by J. Patel.

5.6 Trap-reduction in films (time-dependant measurements): conductivity, Kelvin probe

Fig. 5.7a shows 4-point conductivity probe measurements of $FAPb_{0.5}Sn_{0.5}I_3$ samples with varying amounts of SnF_2 additive over 3 hours in air, after removal from a nitrogen-filled glovebox. With no additive, there is a large rise in the conductivity followed by a fall over the timescale of minutes to hours. Samples prepared with increasing amounts of SnF_2 have a lower initial conductivity, a longer conductivity rise and a lower maximum. **Fig. 5.7b** shows that this rise stops when taken into an N_2 atmosphere and re-starts from the same conductivity value when removed; this is a non-reversible change, hence it is likely to be an effect of oxygen exposure (moisture is unlikely to be the cause given the measurements on precursor solutions). A sample of $FAPbI_3$ shows no conductivity change over 3 hours. Adding 10% $SnCl_2$ also causes a longer conductivity rise with lower peak value (**Fig. 5.7c**). Adding more $SnCl_2$ than 10% decreases the time taken for the conductivity rise. This could be because $SnCl_2$ is now making the initial film quality poorer not better (as seen from the SEM images), as the studied range of 10-40% $SnCl_2$ is well above the 8% optimum concentration found for devices.

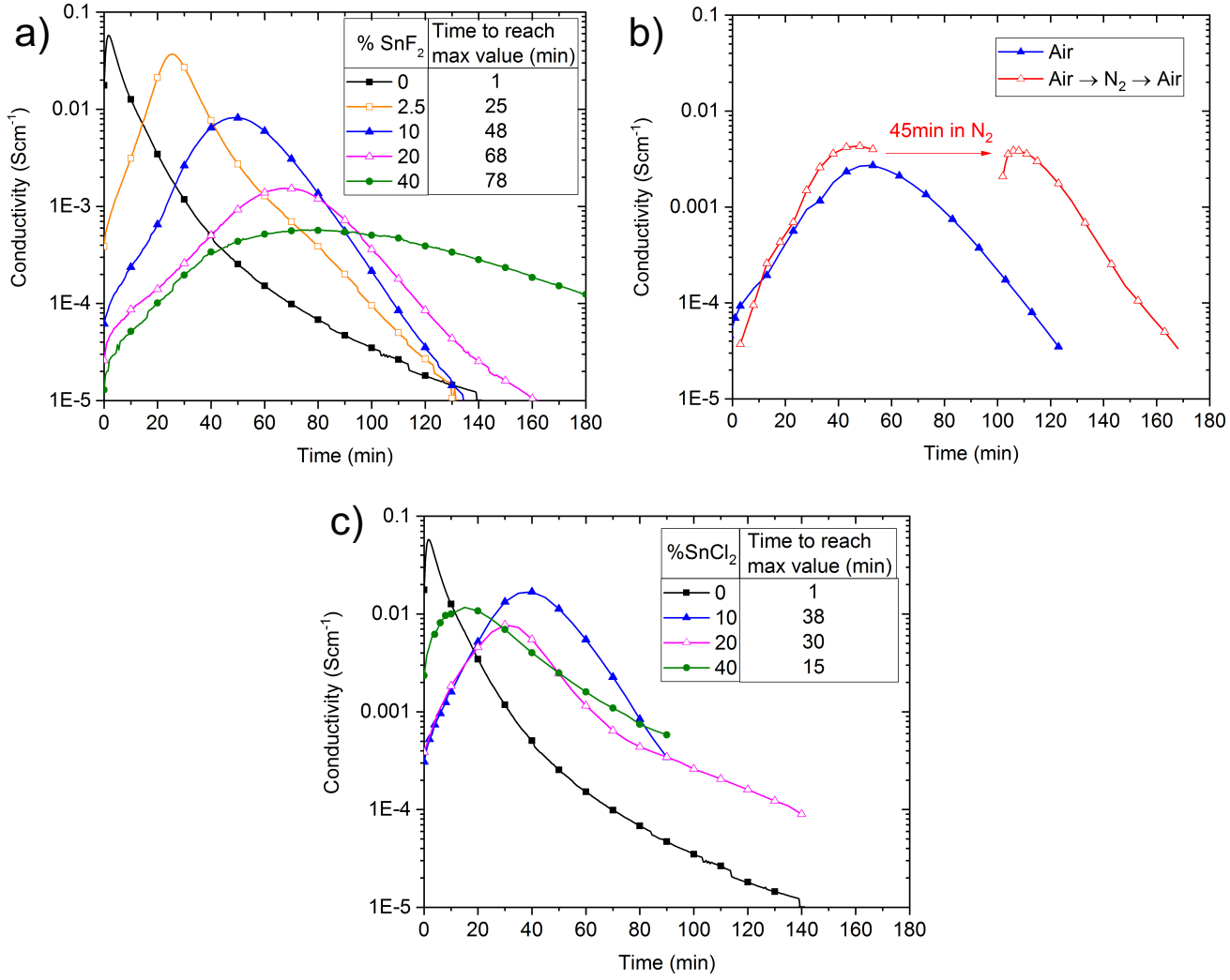


Figure 5.7: a) 4-point conductivity probe measurements of $FAPb_{0.5}Sn_{0.5}I_3$ samples prepared with different amounts of SnF_2 molar excess, over 3 hours in air after removal from an N_2-filled glovebox. b) 4-point conductivity probe measurements of $FAPb_{0.5}Sn_{0.5}I_3$ samples with 10% SnF_2 molar excess, exposed to air after removal from an N_2-filled glovebox, compared to a sample exposed to air for 50 minutes, taken back into an N_2-filled glovebox for 45 minutes, and then returned to air. c) Conductivity of $FAPb_{0.5}Sn_{0.5}I_3$ samples prepared with different amounts of $SnCl_2$ molar excess, over 3 hours in air after removal from an N_2-filled glovebox.

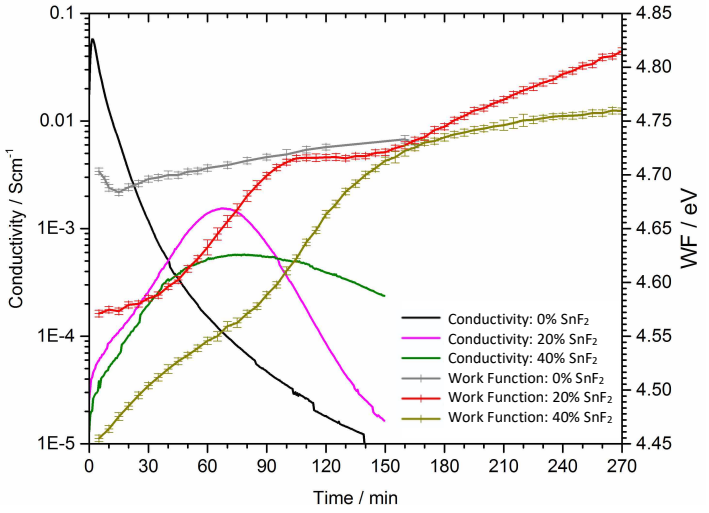


Figure 5.8: Kelvin probe force microscopy work function measurements on $FAPb_{0.5}Sn_{0.5}I_3$ samples prepared with different amounts of SnF_2 molar excess, plotted against the conductivity measurements in Fig. 5.7a.

Fig. 5.8 shows work function measurements on equivalent samples taken by Kelvin probe microscopy over time, plotted alongside the conductivity data from Fig. 5.7a. Samples prepared with SnF_2 initially have a smaller work function and hence are less p-doped than sample with no additives. The sample with 40% excess SnF_2 has a smaller initial work function than the sample with 20% excess SnF_2. Over time, the work functions of the samples with SnF_2 increase rapidly at a similar rate to each other, then flatten off around a value of 4.73eV and continue rising at a slower rate, with the point of regime change taking around 90min for 20% excess SnF_2 and 150min for 40% excess SnF_2. The initial rapid increase in work function occurs at approximately at the same rate for the 20% and 40% samples and is on the same timescale as the conductivity changes. After an initial dip, the work function of the sample with no additives increases at the same slower rate as the samples made with SnF_2, converging at the 4.73eV point. An increase in work function implies the samples are becoming more p-doped, assuming no significant change of the positions of the valence or conduction bands.

These results can be explained by two competing mechanisms: p-doping and degradation, both caused by oxidation. The materials are initially p-type with holes as the dominant carriers[21][70]. Over time, there is an increase in Sn^{2+} vacancies in the lattice due to $Sn^{2+} \rightarrow Sn^{4+}$ oxidation. Vacancy formation creates more free holes, p-doping the material further and leading to a conductivity increase. When the extent of oxidation is severe, degradation dominates and pathways in the lattice for carriers to move could potentially start to break down as many vacancies are formed. SEM images of films after 24h in air show visible pinholes appearing on the scale of 50-100nm, suggesting that on the microscale a conductivity pathway breakdown on the observed timescale of several hours is reasonable. Sn^{4+} that occurs as amorphous SnO_2 could also cause conductivity barriers; XRD of $FAPb_{0.5}Sn_{0.5}I_3$ on the timescale of the conductivity changes shows no extra peaks, so any degradation products must be amorphous rather than crystalline.

The work function measurements show only the p-doping process, which occurs at a fairly constant rate regardless of the initial amount of SnF_2. The conductivity increase also occurs at the same rate regardless of the initial amount of SnF_2. This implies the major effect of SnF_2 is eliminating vacancies during film formation, rather than contributing to some vacancy "healing" or other in-film process; if this were so, with increasing SnF_2 content a slower work function and conductivity increase would be expected, rather than the rates remaining unchanged. With no additives, the initial crystal quality is much poorer; there are many more holes able to conduct and higher initial p-doping. Vacancies and pinholes in the lattice can allow oxygen to percolate through the film much more easily, allowing the degradation process to dominate at much faster timescales and explaining the absence of any conductivity rise in samples with no additive. With additives, a better-quality crystal is formed initially; there are many fewer initial vacancies and therefore holes, so the p-doping level and conductivity are initially lower, and it takes longer for the degradation process to dominate.

Fig. 5.9a shows conductivity measurements under different light intensities. Films measured under an AM1.5 solar simulator, a 0.25 sun LED, ambient and in the dark show a slower and smaller rise in conductivity the lower the light intensity. Under light, the traps are filled and the carrier density will be much greater, leading to higher overall maximum conductivity. Additionally, raising the Fermi level under light will lower the activation energy for the oxidation process, making the degradation occur much faster. The timescale of this effect will be slower in devices, as n or p type layers will provide some protection for the perovskite against oxidation. **Fig. 5.9b** shows conductivity measurements on perovskite samples fabricated on different n and p type layers. PTAA and C_{60} were used because they have lower conductivity than both PEDOT, PCBM and the perovskite layer, ensuring the conductivity of only the perovskite thin film is measured, and not the n and p type materials. With no additive, the degradation process dominates at a rate that is fairly independent of the n and p type layer. With 20% molar excess SnF_2, results on PTAA show a smaller conductivity rise, as most holes will be extracted into the PTAA and not be able to conduct through the perovskite. Results on C_{60} are similar to glass, showing that electrons are the minority carriers and do not significantly affect conductivity.

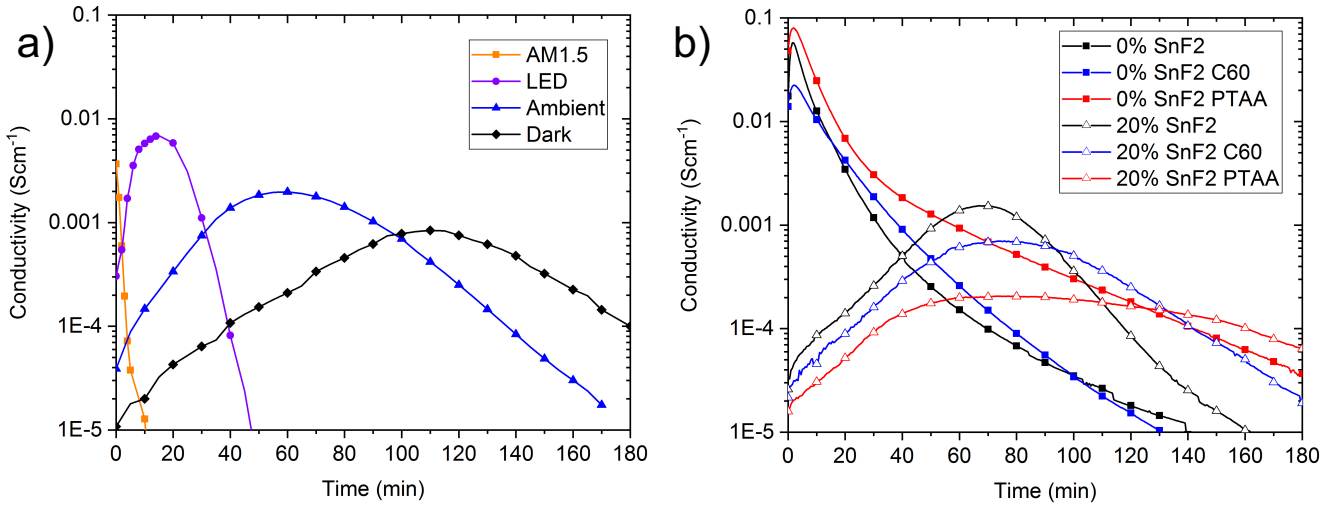


Figure 5.9: a) 4-point conductivity probe measurements of $FAPb_{0.5}Sn_{0.5}I_3$ samples prepared with 20% molar excess SnF_2, over 3 hours in air after removal from an N_2-filled glovebox, under an AM1.5 solar simulator, 0.25 sun LED, ambient light, and in the dark. b) 4-point conductivity probe measurements of $FAPb_{0.5}Sn_{0.5}I_3$ samples prepared on glass, C_{60} and PTAA, with 0% and 20% molar excess SnF_2, over 3 hours in air after removal from an N_2-filled glovebox.

5.7 Conclusion

Used as an additive in mixed Sn-Pb perovskite fabrication, SnF_2 has a function as a reducing agent in solutions, and a tin vacancy compensator in films. Precursor solutions are often Sn^{2+} deficient; Sn^{2+} has been converted to Sn^{4+}, probably from some degradation of precursors. Films made from these solutions are also Sn deficient from EDX and contain Sn^{2+} vacancies. Adding SnF_2 in solution adds more Sn^{2+}, rebalancing the Sn:Pb stoichiometry and allowing film formation with a Sn:Pb ratio closer to 1:1. On SnF_2 addition in solutions, an orange to yellow colour change is caused by I_3^- reduced to I^- by Sn^{2+}, rebalancing the I^- stoichiometry. SnF_2 slows the time taken for I_3^- production on air exposure and makes the solutions more resistant to oxidation.

SnF_2 addition leads to thicker perovskite films with less pinholes and a larger average grain size. They have longer photoluminescence lifetimes, mobilities and diffusion lengths, implying fewer bulk defects such as Sn^{2+} vacancies. The reduction of these vacancies leads to a lower initial p-doping level from Kelvin probe measurements, and allows increased charge collection in solar cells, especially from short wavelength photons. EDX and XRD measurements imply the secondary phase "shards" seen in SEM which appear at higher SnF_2 concentrations are likely to be made of SnF_2, and not another degradation product such as SnO_2 or SnF_4.

Kelvin probe measurements over time in air show p-doping increasing in the films, leading to a conductivity rise then a fall as film degradation dominates. The p-doping rate is independent from the SnF_2 concentration, so SnF_2 is likely to eliminate Sn^{2+} vacancies during film formation rather than any in-film vacancy "healing" process. It takes longer for the degradation to dominate the p-doping mechanism in films which contain more SnF_2, probably because the reduced number of vacancies and pinholes in the lattice leave fewer percolation pathways for oxygen ingress, and so the onset of degradation will be slower.

$FASn_{0.5}Pb_{0.5}I_3$ inverted solar cells fabricated with an SnF_2 additive have better reproducibility thanks to a reduced sensitivity to changes in the processing environment, improved SPO and less hysteresis. The optimum SnF_2 concentration varies between batches, probably due to varying amounts of initial degradation of the precursor salts or solutions. However, solar cell performance parameters show good tolerance to a wide range of SnF_2 concentrations, with only a 3% drop in SPO between 2.5% and 40% SnF_2 molar excess.

Although a $SnCl_2$ additive can achieve similar improvements in perovskite film quality and produce solar cells of almost equivalent performance as SnF_2, it is less appropriate for use as an Sn^{2+} vacancy compensator because films are much more sensitive to the precise concentration of $SnCl_2$, probably because $SnCl_2$ is a stronger reducing agent than SnF_2. The best-performing solar cells fabricated here had SPO values of 12.5% with 2.5% molar excess SnF_2, lower than the 20% SnF_2 standard in the literature, and 9.6% with 8% molar excess $SnCl_2$. As many different Sn-containing precursors and multiple-cation combinations of MA, FA and Cs are currently being studied, performing an SnF_2 additive dependence for a particular preparation route is advisable in order to achieve the very highest performance in devices based on Sn-Pb perovskites.

6. Organic and inorganic cation screening for mixed tin-lead perovskite solar cells

6.1 Introduction

Most of the research focus on Sn and Sn-Pb perovskites was initially limited to a single cation, methylammonium CH_3NH_3 (MA)[19][35]. As demonstrated in chapter 4, use of the formamidinium $CH(NH_2)_2$ (FA) cation should provide increased thermal stability, and can lead to improved film quality and high solar cell performance using a complex-assisted gas quenching fabrication method. Changing this A-site cation is possible without dramatically changing material properties because the main bonds that contribute to the band structure of these materials are from the metal and halide and not the A-site cation, as described in section 2.4. Recently, combinations of MA and FA cations with Sn-Pb perovskites have demonstrated impressive efficiency results of over 20%[49]. A small addition of Cs has been shown to boost the performance and stability of Pb based perovskites[71][72][73]. In chapter 4 a similar performance boost on Cs substitution for FA in Sn-Pb perovskites was described, with a champion low-band gap device fabricated at Stanford containing 25% Cs, and champion device fabricated at Oxford with 5% Cs. Adding just 1% Cs causes a large increase in the short-circuit current density J_{sc}, without a significant effect on other thin film properties. The effects of both MA and Cs addition to FA-based Sn-Pb perovskites are therefore clearly worthy of further investigation.

This chapter presents a screening study examining the compositional space between the three A-site cations (FA:MA:Cs) in mixed Sn-Pb perovskites, investigating thin film band gaps in order to determine if anomalous band gap bending is observed as is the case on the B-site between Sn:Pb, and to find the material with the lowest accessible band gap for tandem solar cell applications, both in the (FA:Cs)(Sn:Pb) compositional space (which has produced the high-performing devices shown in previous chapters) and also in the more general (FA:MA:Cs)$Sn_{0.5}Pb_{0.5}I_3$ compositional space. Materials are fabricated using a universal deposition protocol, focussing especially on the Cs cation and if it can substitute into the crystal lattice from 0 to 100% Cs; Cs addition into perovskites containing organic cations has been shown to improve solar cell performance and also increase thermal stability, so if this compositional space is accessible these materials present a promising area for further experiments[30]. Finally, solar cells are fabricated using perovskites over the whole compositional range of A-site cations, in order to investigate if power can be generated from new materials in this space and which compositions might be worthy of further detailed study.

6.2 Substitution of Cs: fabrication of $FA_{1-y}Cs_ySn_xPb_{1-x}I_3$ perovskites

As a preliminary study, the complex-assisted gas quenching method was used to make a series of $FA_{1-y}Cs_ySn_{0.5}Pb_{0.5}I_3$ perovskite films with y=0 to 1 (pure FA to pure Cs). **Fig. 6.1a** shows XRD measurements on these films. The 2theta value of the 110 perovskite peak decreases with increasing Cs content, as would be expected, since substituting more of the larger FA^+ cation with the smaller Cs^+ cation corresponds to a decrease in lattice parameter and crystal size. It can be seen that all compositions make a crystalline perovskite; the full compositional range between FA and Cs is available to be studied in Sn-Pb perovskites, which allow a larger % Cs to be substituted into the lattice than in pure Pb based perovskites.

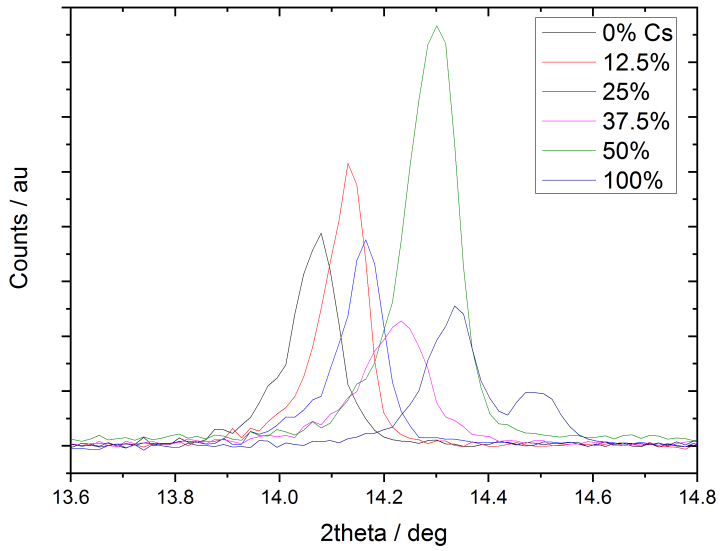


Figure 6.1: X-ray diffraction (XRD) pattern of $FA_{1-y}Cs_ySn_{0.5}Pb_{0.5}I_3$ samples, magnified around the 110 perovskite peak.

Fig. 6.2 shows preliminary results from steady-state photoluminescence measurements of $FA_{1-y}Cs_ySn_xPb_{1-x}I_3$ perovskites, with the FA(Sn:Pb)I_3 series shown in Fig. 4.2c along the x axis, and the red line showing the (FA:Cs)$Sn_{0.5}Pb_{0.5}I_3$ series studied in XRD. With FA(Sn:Pb)I_3 or MA(Sn:Pb)I_3 band gap bending with increasing Sn addition is observed, with the lowest band gaps around 60% Sn content[35]; however with Cs(Sn:Pb)I_3 no band gap bending and a constantly increasing band gap from $CsSnI_3$ to $CsPbI_3$ is seen. The most detail on this plot is from the Sn-rich side of the compositional space; the Pb-rich compositions were not investigated as these perovskites with 0.5-30% Sn have been shown to be optoelectronically defective with pure FA (section 4.5). If in future experiments devices were fabricated over this Pb-rich region, care should be taken with solar simulator calibration and calculation of mismatch factor due to the large change in band gap. The Sn-rich parts of the compositional space have the lowest band gaps and are most applicable to tandem perovskite devices. The local minimum band gap of 1.23eV occurs at 60% Sn, 25% Cs.

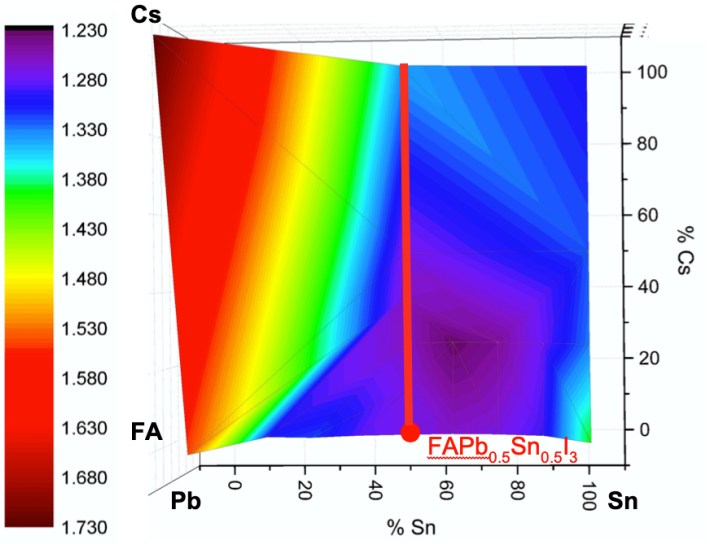


Figure 6.2: Contour plot of extracted band gaps from steady-state photoluminescence spectroscopy (SSPL) measurements on $FA_{1-y}Cs_ySn_xPb_{1-x}I_3$ thin films, with Sn content on the x-axis and Cs content on the y-axis. The red line shows the band gaps of the series of films with 50% Sn content examined in Fig. 6.1.

6.3 Triple cation perovskites: thin film properties

To extend the previous analysis to include the MA cation, the Sn:Pb ratio was fixed at 50:50 and seven different representative compositions of A-site cations were studied: pure FA, MA, and Cs; 50:50 blends of FA-MA, FA-Cs and MA-Cs; and a 33% "triple cation" blend of FA-MA-Cs. **Fig. 6.3a** shows a diagram of the different compositions for this triple cation screening.

All films were fabricated using the complex-assisted gas quenching method, and the processing parameters of gas quenching time and annealing time were optimised to produce the best film quality from scanning electron microscope (SEM) analysis. The method set out for $FASn_{0.5}Pb_{0.5}I_3$ in chapter 5 were used as a starting point, with optimised processing parameters for each of the seven compositions listed in section 3.1.3. FA, Cs, and FA-MA-Cs benefitted from annealing for 20min, MA and FA-MA required no annealing at all, while MA-Cs films were best with a short 1min anneal. The film quality improved with less annealing for MA, FA-MA and MA-Cs as the MA cation is more volatile than FA or Cs, so care must be taken when annealing so as not to drive off the MA cation.

FA-Cs is a special case: **Fig. 6.3b** shows an SEM image of a thin film of FA-Cs made using gas quenching; rather than a smooth continuous layer, large crystallites can be seen on the surface of the film, indicating a possible structural instability at this composition to this processing method. None of the other 6 compositions in the series were as sensitive to the optimum deposition parameters. It was found that in order to form a uniform film of FA-Cs, no gas quenching but a short 1min anneal was required. It can also be seen from the XRD measurements in Fig. 6.1 that the sample with 50% Cs has a higher peak and is more crystalline than the other compositions; further work is required to determine if this is an intrinsic instability in the material at this composition which leads to this phase separation.

Fig. 6.3c shows SEM images of thin films made from all seven compositions of (FA:MA:Cs), with processing parameters optimised for each composition. All compositions apart from pure Cs show good coverage and are relatively pinhole-free, implying the complex-assisted gas quenching method is an appropriate universal deposition protocol for these films. The FA-MA film has a smaller grain size than pure FA, and in most other compositions individual grains cannot be made out. The more optimised FA-Cs film shown here still has a non-uniform structure. The pure Cs film shows some significant pinholes; more optimisation is likely to be required to create a pinhole-free continuous film.

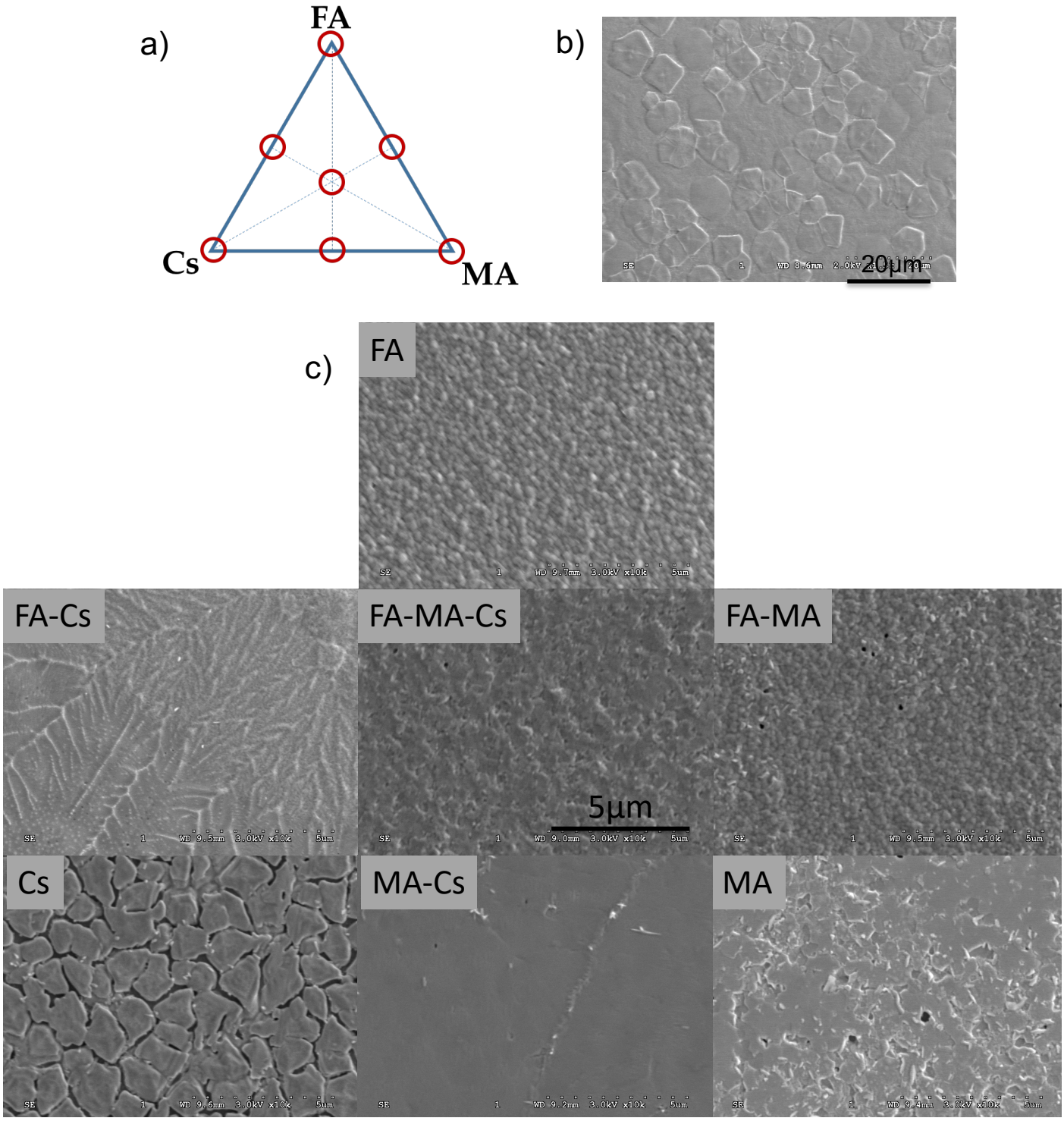


Figure 6.3: a) Diagram of the seven compositions of (FA:MA:Cs)$Sn_{0.5}Pb_{0.5}I_3$ perovskite films with different A-site cations examined during this study: pure FA, MA, and Cs; 50:50 blends of FA-MA, FA-Cs and MA-Cs; and a 33% blend of FA-MA-Cs. b) Scanning electron microscope (SEM) image of FA-Cs thin film prepared using non-optimised processing parameters. c) SEM images of thin films of all seven compositions using optimised processing parameters.

Fig. 6.4a shows XRD measurements of thin films of all seven compositions of (FA:MA:Cs), centred on the 110 perovskite peak, and extracted 2theta peak positions. All the compositions are able to form a crystalline perovskite, with the 110 peak of the Cs and FA-Cs samples lower in intensity possibly due to differences in crystal orientation. The peak positions are consistent with the relative cation sizes: the largest cation, FA, has the lowest 2theta value, the smallest cation Cs has the largest value, with MA in between. All the cation mixtures have peak positions in between the two end point cations. The Cs is therefore incorporating into the lattice at all different combinations of these cations.

Fig. 6.4b shows steady-state photoluminescence (SSPL) spectra for all seven compositions of (FA:MA:Cs), and **Fig. 6.4c** shows ultraviolet-visible (UV-vis) absorption measurements on the same films. **Fig. 6.4d** shows extracted band gaps from the SSPL and absorption measurements, with two different extraction methods from the UV vis data, via a Tauc plot and via direct measurement of the absorption edge onset. The band gaps are broadly consistent, with the highest values for pure Cs and lowest values for pure MA. Adding Cs widens the band gaps of the organic cation combinations by 0.02-0.05eV. All the A-site cation mixtures have band gaps in between the two end point cations, and no band gap bending is observed as is seen at the B-site with FA(Sn:Pb)I_3 or MA(Sn:Pb)I_3. The crystal size from XRD and the band gap are not necessarily related; while FA has the largest lattice parameter value it does not have the lowest band gap, although that is the only exception to the rule, and generally the larger the crystal size, the lower the band gap.

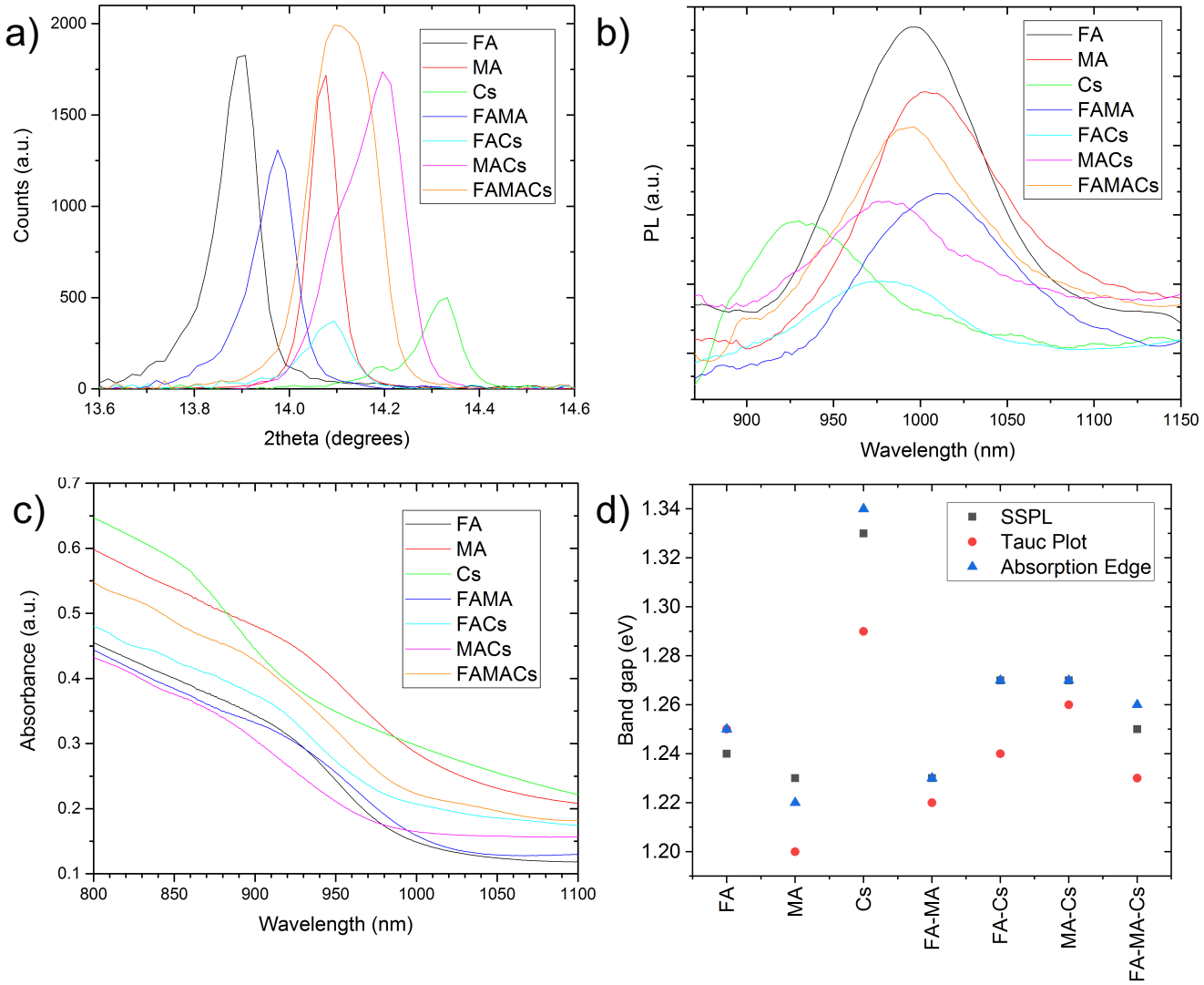


Figure 6.4: a) X-ray diffraction (XRD) measurements of the seven (FA:MA:Cs)$Sn_{0.5}Pb_{0.5}I_3$ perovskite thin films examined during this study. b) Steady-state photoluminescence (SSPL) measurements of these films. c) Ultraviolet-visible (UV-vis) absorption measurements of these films. d) Extracted band gaps from the SSPL peak position 6.4b, and from the absorption 6.4c via Tauc plot (assuming direct band gap) and absorption edge onset.

6.4 Triple cation perovskites: solar cells

Fig. 6.5a-e show performance parameters for inverted planar solar cells made with all seven compositions of (FA:MA:Cs) perovskite. **Table 6.1** shows solar cell performance parameters and **Fig. 6.6** shows current density – voltage (J-V) curves for the best performing devices of each composition. All compositions apart from FA-Cs are able to generate power, showing that the many different cation combinations within this compositional space are worth exploring in future work. Full optimisation of each material including thickness variation of each absorber composition, rather than just this simple proof-of concept processing optimisation based on SEM analysis, could lead to high solar cell performance in new classes of low band gap perovskite materials.

As expected, the devices with pure FA perovskite performed the best, with maximum power conversion efficiency (PCE) values of 13.8%. As described in chapter 4, the gas quenching method as well as the other solar cell layers have previously been carefully optimised for this composition, so good performance as a control sample would be expected. The pure MA perovskite device gives a 4.3% PCE, comparable with values in the literature, without us having undergone significant optimisation for this specific material[35]. $MASn_{0.5}Pb_{0.5}I_3$ solar cells do show a large spread in performance values, this could be because they are likely to be more sensitive to heat and air exposure than other cation combinations.

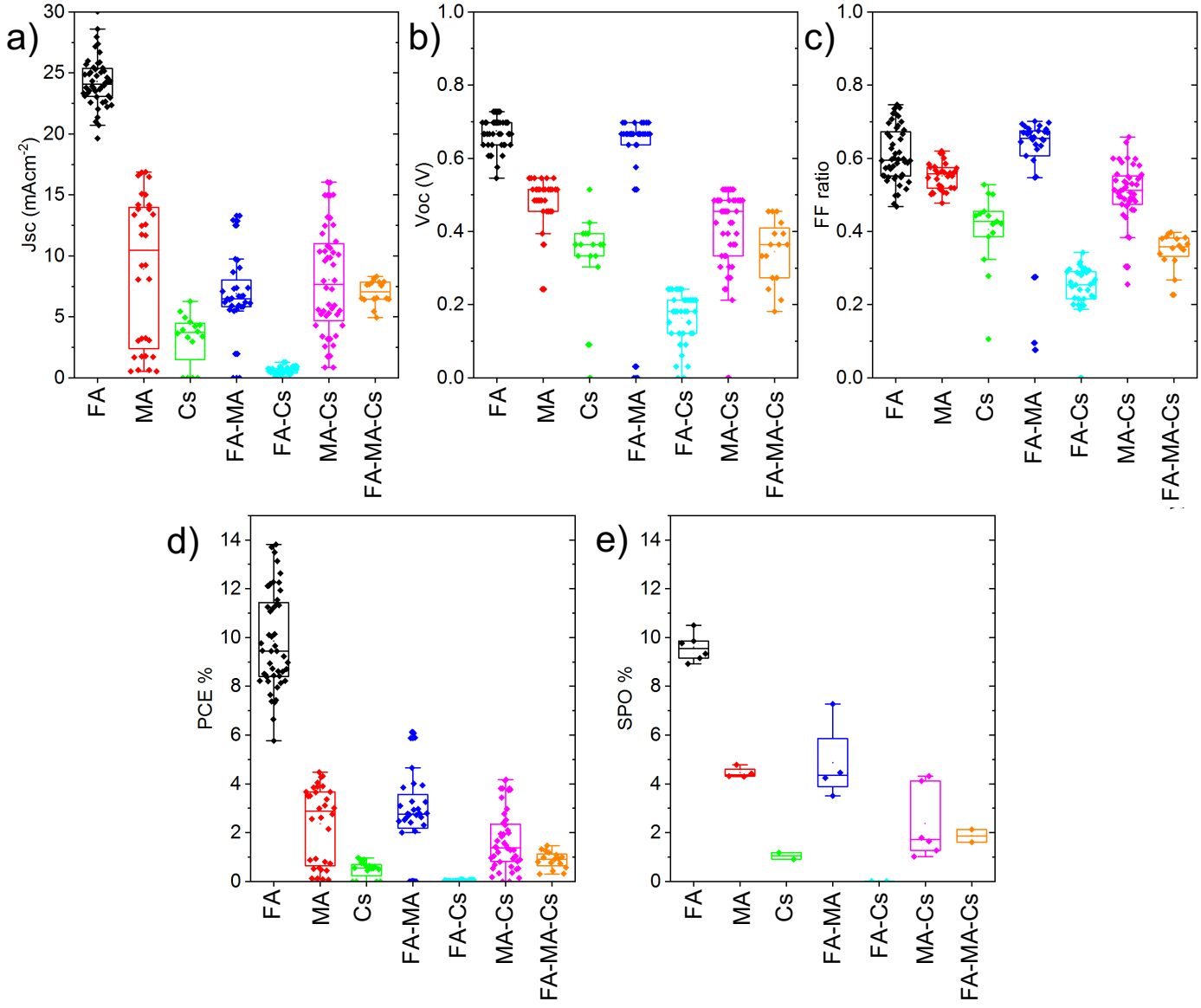


Figure 6.5: Solar cell performance parameters a) short-circuit current density (J_{sc}), b) open-circuit voltage (V_{oc}), c) fill factor (FF), d) power conversion efficiency (PCE), and e) stabilised power output (SPO), for devices made using (FA:MA:Cs)$Sn_{0.5}Pb_{0.5}I_3$ perovskite, with seven different A-site cation combinations.

	FA	MA	Cs	FA-MA	FA-Cs	MA-Cs	FA-MA-Cs
PCE %	13.8	4.3	1.0	8.7	0	4.2	1.5
SPO %	10.5	4.8	1.2	7.3	-	4.3	2.1
J_{sc}(mAcm^{-2})	25.9	16.8	6.3	18.3	-	15.0	8.3
V_{oc} (V)	0.73	0.52	0.42	0.76	-	0.52	0.45
FF	0.74	0.51	0.53	0.68	-	0.56	0.40

Table 6.1 Solar cell performance parameters for best-performing solar cells with seven combinations of A-site cations. Uncertainties in each measurement (standard deviation of device performance parameters) are illustrated in Fig. 6.5.

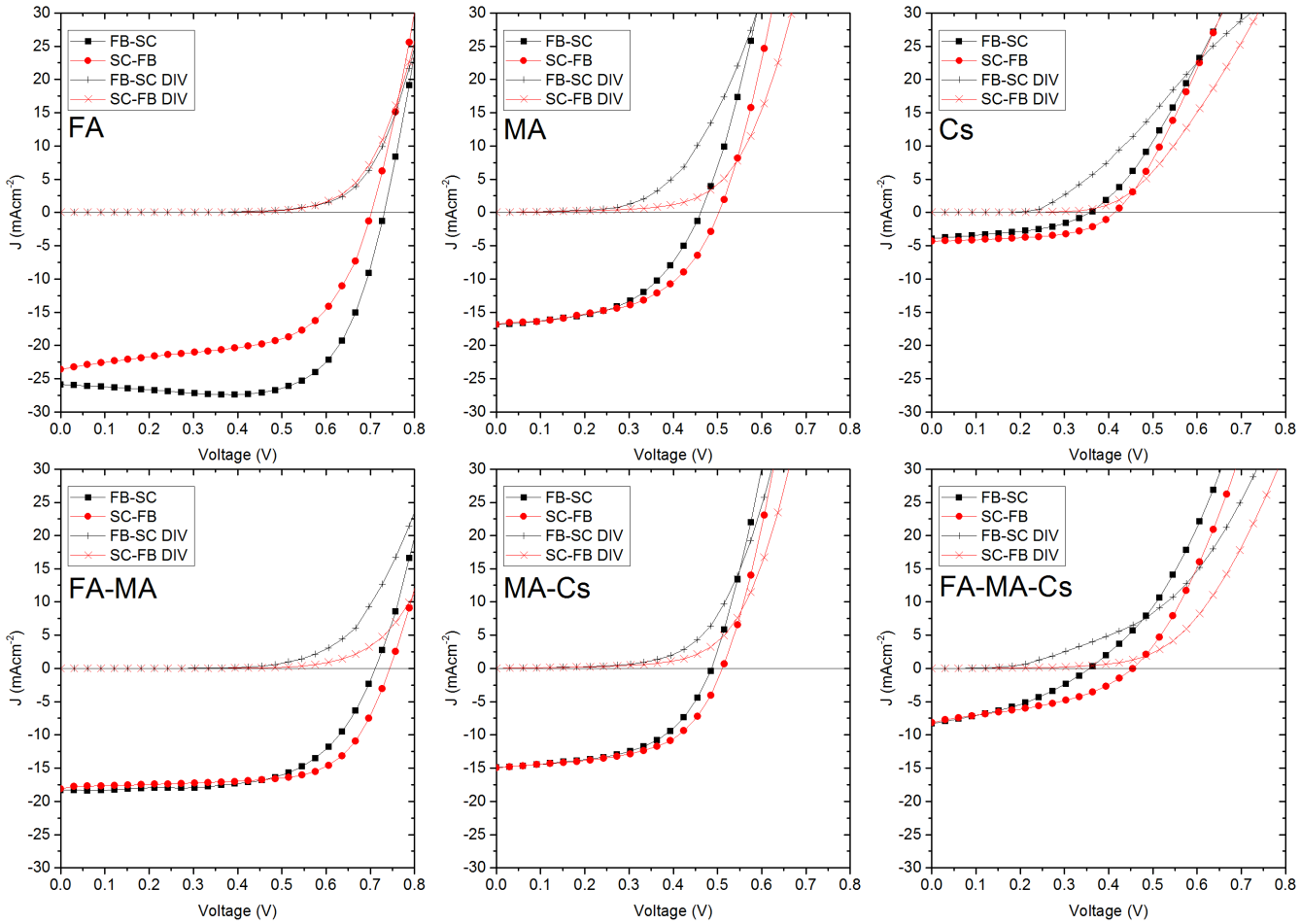


Figure 6.6: Current density - voltage (J-V) curves for best-performing devices of each composition, excluding FA-Cs, which did not make a working solar cell.

The FA-MA perovskite shows a good PCE and a particularly good V_{oc}, higher than the champion pure FA device. Even in this proof of principle screening it is clear this composition is capable of high performance if the J_{sc} value could be improved. Thickness optimisation of the perovskite layer for each different composition was not carried out in this proof-of-principle study; this would be an obvious first step to improve the current if the thickness of this particular composition is too low for efficient carrier absorption. Increasing the carrier diffusion length through a vacancy compensation method with an additive as described in chapter 5 would also be a promising route to further improvement of J_{sc}; indeed, this composition has attracted research interest recently, and with further processing optimisation and a guanidinium thiocyanate (GuaSCN) additive has achieved over 20% efficiency[49].

The pure Cs device ($CsSn_{0.5}Pb_{0.5}I_3$) is to the best of the author's knowledge one of the first working solar cell devices made from a completely inorganic perovskite with mixed Sn-Pb. Although the PCE is only 1%, it demonstrates that an organic cation is not essential for solar cell operation, as has been shown with $CsPbI_3$ perovskites[30]. Low J_{sc} values could again potentially be improved by thickness optimisation. The mixed MA-Cs device shows similar performance to the pure MA device; adding Cs to MA perovskites may improve their thermal stability and reduce sensitivity to oxidation once optimised, as has been seen in Pb-based solar cells. Given the poor reproducibility of the $MASn_{0.5}Pb_{0.5}I_3$ devices, Cs addition could solve some of these problems once optimised.

Devices based on FA-Cs perovskite ($FA_{0.5}Cs_{0.5}Sn_{0.5}Pb_{0.5}I_3$) did not make a working solar cell. This is surprising as the best device results in these experiments have been when small amounts of Cs are added to FA perovskites, such as $FA_{0.95}Cs_{0.05}Sn_{0.5}Pb_{0.5}I_3$ or $FA_{0.75}Cs_{0.25}Sn_{0.5}Pb_{0.5}I_3$, discussed in chapter 4. It was discussed in section 6.3 that processing this composition using the gas quenching method was challenging due to a potential structural instability at this high Cs content. Triple cation FA-MA-Cs devices showed slightly better performance than pure Cs, but it is surprising the performance is not higher, given good results with 25% Cs and pure FA; it could be that the structural instability described above may start at Cs content as low as 33%. This is an area worthy of further study.

6.5 Conclusion

Thin films of perovskites in the compositional space (FA:MA:Cs)(Sn:Pb)I_3 were fabricated using a universal gas quenching deposition protocol. The lowest band gap material in the (FA:Cs)(Sn:Pb)I_3 compositional space was found at 1.23eV for 60% Sn, 25% Cs, as measured from the SSPL peak. Preliminary SSPL results imply that no anomalous band gap bending occurs within Cs(Sn:Pb)I_3 perovskites; the band gap decreases continuously from $CsPbI_3$ to $CsSnI_3$. SSPL and absorption measurements of seven (FA:MA:Cs)$Sn_{0.5}Pb_{0.5}I_3$ compositions show low band gaps in the compositional space between 1.23-1.27eV, apart from $CsSn_{0.5}Pb_{0.5}I_3$, which has a higher band gap around 1.33eV. The lowest band gap of these compositions was 1.23eV for $MASn_{0.5}Pb_{0.5}I_3$; a slightly lower gap may be achievable by altering the Sn:Pb ratio from 50:50 or adding small amounts of FA or Cs. No band gap bending is observed using A-site cations, unlike the mixed-metal B-site (Sn:Pb) series. This screening study has highlighted new perovskites with even lower band gaps than the standard cation combinations used in the literature, with applications in all-perovskite tandem solar cell devices.

All the studied A-site cation combinations of (FA:MA:Cs)$Sn_{0.5}Pb_{0.5}I_3$ show almost full coverage from SEM and good crystallinity from XRD, with lattice parameters as expected from cation size. Substituting Cs for FA in the crystal lattice was possible from 0 to 100% Cs, with all compositions making a crystalline perovskite with decreasing crystal size on Cs addition. A potential structural instability around 50% Cs content requires careful processing optimisation in order to achieve a smooth film. These observations should inform future experiments seeking low band gap perovskites with particular advantageous properties such as improved thermal and moisture stability.

Solar cell devices fabricated from (FA:MA:Cs)$Sn_{0.5}Pb_{0.5}I_3$ are all able to generate power apart from $FA_{0.5}Cs_{0.5}Sn_{0.5}Pb_{0.5}I_3$, possibly due to the structural instability described above. Some combinations show surprisingly good performance, particularly $FA_{0.5}MA_{0.5}Sn_{0.5}Pb_{0.5}I_3$ and $MA_{0.5}Cs_{0.5}Sn_{0.5}Pb_{0.5}I_3$. While 50% Cs addition appears to be too high to achieve good solar cell performance, this study suggests that adding smaller amounts of Cs to the highest performing devices in the literature currently based on (FA:MA)(Sn:Pb)I_3 perovskites is possible. This could provide a similar performance boost as observed on Cs addition to $FAPbI_3$ and $FASn_{0.5}Pb_{0.5}I_3$ solar cells, attributed to reduced trap density[72][22]. Since perovskites can be fabricated throughout the whole A-site compositional space, in future work it could also be possible to tailor material properties such as band gap or thermal stability for specific applications by choosing a (FA:MA:Cs) cation combination that gives these properties, and optimising the solar cell layers and material processing parameters to achieve higher efficiency values than have been demonstrated in this simple optimisation study.

7. Conclusions and outlook

The main aims of this thesis have been to investigate processing methods, the role of additives and choice of cations to improve the optoelectronic properties and solar cell performance of low bandgap mixed tin-lead perovskite semiconductor materials. This work has provided improved processing techniques allowing slower perovskite crystallisation for better film quality, an understanding of how additives can control bulk vacancies acting as trap states in the perovskite, and a compositional study that acts as a proof of principle for fabrication of new high performance materials. As Sn-Pb perovskites offer the only known route to achieve band gaps below 1.5eV, including the 1.34eV optimal band gap for single-junction devices and the ~1.2eV band gap for bottom-cell silicon replacement in perovskite-perovskite tandem devices, overcoming some of these challenges in Sn-Pb perovskite semiconductor fabrication is crucial[14].

Chapter 4 addressed the problem of rapid crystallisation of Sn-Pb perovskites during film formation, which led to poor film morphology. Using the FA cation rather than MA, it was shown that a mixed solvent of DMF:DMSO together with an appropriate antisolvent or a stream of nitrogen allows slower perovskite crystallisation and the fabrication of pinhole-free (FA:Cs)(Sn:Pb)I_3 thin films with low band gap, long diffusion length and high mobility. These two techniques were termed precursor phase antisolvent immersion and complex-assisted gas quenching. An optoelectronically defective region was identified between 0.5-20% Sn content (1.35-1.5eV band gap), suggesting that in this region Sn is introducing sub-band gap trap states into the material. These methods led to a demonstration of some of the first high efficiency single-junction cells and perovskite-perovskite tandem devices[22], and similar techniques have now been used in both pure-Sn and mixed Sn-Pb perovskites, with single-junction results of over 20%[49] using a Sn-Pb perovskite containing both FA and MA, and monolithic perovskite-perovskite tandem devices with efficiencies of up to 24.8%[52]. This highlights the importance of the processing solvent in these materials in order to achieve high performance.

In chapter 5, the instability of tin in its Sn^{2+} state leading to Sn^{2+} vacancies within mixed Sn-Pb perovskites was addressed. SnF_2 and $SnCl_2$ additives were demonstrated to function both as reducing agents in precursor solutions, and as vacancy compensators within the perovskite thin films. As reducing agents they rebalanced the iodide stoichiometry within precursor solutions, and as vacancy compensators they provided Sn^{2+}, rebalancing the Sn:Pb stoichiometry and improving the morphology and optoelectronic quality of the perovskite layer, leading to lower initial p-doping. It was shown that secondary phase "shards" are composed of SnF_2, and high efficiency low band gap solar cells were fabricated with both additives, which showed a good tolerance to precise SnF_2 content but were less tolerant to precise $SnCl_2$ content. Thin films of Sn-Pb perovskites were examined over time in air, and it was shown how additives can affect the balance between p-doping and degradation mechanisms within the films and slow the onset of degradation. Prior to widespread use of SnF_2, the best performing Sn-based device was made using a meso-superstructured architecture, where the short electron diffusion length was not such an issue as electrons had only a short distance to travel to reach the mesoporous TiO_2 scaffold[19]. In planar cells these additives are crucial in order to improve the electron diffusion length and allow improved charge collection. In all future work on Sn-Pb perovskites it would be advisable to perform an SnF_2 additive dependence for a particular preparation route to achieve the very highest device performance.

In chapter 6, a compositional screening study of Sn-Pb perovskites with different combinations of A-site cations MA, FA and Cs was presented, laying foundations for future work on new low band gap materials. It was demonstrated that all compositions can be fabricated by a simple universal deposition protocol (complex-assisted gas quenching) and the resulting thin film properties and band gaps are consistent with substitution of these three cations into the lattice with no anomalous band gap bending. This produced an almost fully accessible compositional space, although a compositional instability with 33-50% Cs substitution for FA was demonstrated; further work is required to determine if this is an intrinsic instability in the material at this composition. Solar cells of each

composition were demonstrated, and compositions with particularly good performance identified as worthy of further study. These included a combination of MA and FA; recently this composition has produced the highest performing mixed Sn-Pb solar cell to date, using a similar additive addition optimisation method as was demonstrated in chapter 5[49]. This study lays a foundation for future tailoring of material properties such as band gap or thermal stability for specific applications, by choosing a cation combination that gives these properties and optimising the solar cell layers and material processing parameters in order to achieve high efficiency.

There are several further experiments that would be beneficial to deepen understanding of these low band gap perovskite materials and their function in solar cells. While proof of concept all-perovskite 2-terminal and 4-terminal tandem solar cells have been demonstrated in chapter 4, scaling these devices to larger active areas necessary for real-world applications while retaining high efficiency still remains challenging. The degradation mechanism that causes a conductivity decrease in perovskite films over time in air observed in chapter 5 has not been comprehensively investigated; in-situ measurements on thin films and devices in controlled environments under the influence of light, heat, moisture, oxygen and combinations of these factors would be valuable in order to understand the underlying mechanics. Analysing the Sn^{4+} concentration in the film during degradation using a combination of XPS and EDX would determine if the degradation pathway proceeds via SnO_2 or SnI_4; it has been proposed that as Sn^{2+} vacancies are created SnI_4 gas leaves the film, but its boiling point of 348°C is high for it to be spontaneously evolved in this way[59].

Full investigation of the most promising materials demonstrated in chapter 6 by optimising perovskite thickness and optoelectronic properties such as PL and mobility for devices of each absorber composition (as opposed to our simple analysis based on SEM) could lead to high solar cell performance in new classes of low band gap perovskite materials. Further detailed measurements of the observed structural instability around $FA_{0.5}Cs_{0.5}Sn_{0.5}Pb_{0.5}I_3$ are required in order to investigate whether this is purely a processing issue or something more fundamental to this material composition. Comparison of the thermal and moisture stability of Cs-containing perovskites in the (FA:MA:Cs)(Sn:Pb)I_3 compositional space would confirm if Cs addition provides the same beneficial properties in these areas as those seen in the pure Pb system, in addition to the observed boost in solar cell performance.

While methods to improve initial material quality have been demonstrated, probably the most important issue that has not been addressed in detail is the stability over time of these materials. Solar cell modules must be guaranteed to last 25 years and be subject to rigorous stress and ageing tests including temperature, humidity, and ultraviolet light over many hours. Perovskite materials containing tin have been shown to be extremely sensitive to air exposure, and all precursor preparation and device fabrication must be undertaken within a nitrogen atmosphere. Rigorous encapsulation techniques and assessment of the stability of these low band gap materials within modules over a long period of time will be essential to ensure that these instabilities will not limit the commercial viability of these materials.

In summary, this thesis has presented several conclusions to improve low band gap perovskite solar cell materials that could enhance the commercial viability of these devices in the future. While there are still significant barriers to real-world application of these materials including their stability over time, if these challenges can be overcome, low band gap perovskite solar cells could make a significant contribution to the rapid worldwide deployment of renewable energy that is necessary to combat man-made climate change.

8. References

[1] J. Jean, P.R. Brown, R.L. Jaffe, T. Buonassisi, V. Bulovic, *Energy Environ. Sci.* **2015**, *8*, 1200.
[2] D. Spencer, *BP Stat. Rev. World Energy* **2019**.
[3] W. Shockley, H.J. Queisser, *J. App. Phys.* **1961**, *32*, 510.
[4] J. Nelson, *The Physics of Solar Cells*, **2004**.
[5] B.E. Hardin, H.J. Snaith, M.D. McGehee, *Nat. Photonics* **2012**, *6*, 162.
[6] E.H. Sargent, *Nat. Photonics* **2012**, *6*, 133.
[7] J. Nelson, *Mater. Today* **2011**, *14*, 462.
[8] H.J. Snaith, *Adv. Funct. Mater.* **2010**, *20*, 13.
[9] NREL, *Https://Www.Nrel.Gov/Pv/Cell-Efficiency.Html* **2019**.
[10] H.S. Jung, N.-G. Park, *Small* **2014**, *11*, 10.
[11] H.J. Snaith, *Nat. Mater.* **2018**, *17*, 372.
[12] A. Abate, J.P. Correa-Baena, M. Saliba, M.S. Su'ait, F. Bella, *Chem. - A Eur. J.* **2018**, *24*, 3083.
[13] Y. Rong, Y. Hu, A. Mei, H. Tan, M.I. Saidaminov, S. Il Seok, M.D. McGehee, E.H. Sargent, H. Han, *Science* **2018**, *361*, eaat8235.
[14] S.D. Stranks, H.J. Snaith, *Nat. Nanotechnol.* **2015**, *10*, 391.
[15] M. Hoerantner, T. Leijtens, G. Eperon, M. Ziffer, M.G. Christoforo, H. Snaith, *ACS Energy Lett.* **2017**, *2*, 2506.
[16] I. Chung, B. Lee, J. He, R.P.H. Chang, M.G. Kanatzidis, *Nature* **2012**, *485*, 486.
[17] D. Fabini, *J. Phys. Chem. Lett.* **2015**, *6*, 3546.
[18] A. Babayigit, D. Duy Thanh, A. Ethirajan, J. Manca, M. Muller, H.-G. Boyen, B. Conings, *Sci. Rep.* **2016**, *6*, 18721.
[19] N.K. Noel, S.D. Stranks, A. Abate, C. Wehrenfennig, S. Guarnera, A. Haghighirad, A. Sadhanala, G.E. Eperon, S.K. Pathak, M.B. Johnston, A. Petrozza, L.M. Herz, H.J. Snaith, *Energy Environ. Sci.* **2014**, *7*, 3061.
[20] E.S. Parrott, R.L. Milot, T. Stergiopoulos, H.J. Snaith, M.B. Johnston, L.M. Herz, *J. Phys. Chem. Lett.* **2016**, *7*, 1321.
[21] R.L. Milot, G.E. Eperon, T. Green, H.J. Snaith, M.B. Johnston, L.M. Herz, *J. Phys. Chem. Lett.* **2016**, *7*, 4178.
[22] G.E. Eperon, T. Leijtens, K.A. Bush, R. Prasanna, T. Green, J.T.-W. Wang, D.P. McMeekin, G. Volonakis, R.L. Milot, R. May, A. Palmstrom, D.J. Slotcavage, R.A. Belisle, J.B. Patel, E.S. Parrott, R.J. Sutton, W. Ma, F. Moghadam, B. Conings, A. Babayigit, H.-G. Boyen, S. Bent, F. Giustino, L.M. Herz, M.B. Johnston, M.D. McGehee, H.J. Snaith, *Science* **2016**, *354*, 861.
[23] H.J. Snaith, A. Abate, J.M. Ball, G.E. Eperon, T. Leijtens, N.K. Noel, S.D. Stranks, J.T. Wang, K. Wojciechowski, W. Zhang, *JPCL* **2014**, *5*, 1511.
[24] S. van Reenen, M. Kemerink, H.J. Snaith, *J. Phys. Chem. Lett.* **2015**, 3808.
[25] M.R. Filip, G.E. Eperon, H.J. Snaith, F. Giustino, *Nat. Commun.* **2014**, *5*, 1.
[26] T. Umebayashi, K. Asai, T. Umebayashi, K. Asai, T. Kondo, T. Kondo, A. Nakao, *Phys. Rev. B - Condens. Matter Mater. Phys.* **2003**, *67*, 2.
[27] G. Kieslich, S. Sun, T. Cheetham, *Chem. Sci.* **2015**, *6*, 3430.
[28] G.E. Eperon, S.D. Stranks, C. Menelaou, M.B. Johnston, L.M. Herz, H.J. Snaith, *Energy Environ. Sci.* **2014**, *7*, 982.
[29] P.P. Boix, S. Agarwala, T.M. Koh, N. Mathews, S.G. Mhaisalkar, *J. Phys. Chem. Lett.* **2015**, *6*, 898.
[30] G.E. Eperon, G.M. Paternò, R.J. Sutton, A. Zampetti, A.A. Haghighirad, F. Cacialli, H.J. Snaith, *J. Mater. Chem. A* **2015**, *3*, 19688.
[31] R.J. Sutton, G.E. Eperon, L. Miranda, E.S. Parrott, B.A. Kamino, J.B. Patel, M.T. Hörantner, M.B. Johnston, A.A. Haghighirad, D.T. Moore, H.J. Snaith, *Adv. Energy Mater.* **2016**, 1502458.
[32] J.H. Noh, S.H. Im, J.H. Heo, T.N. Mandal, S. Il Seok, *Nano Lett.* **2013**, *13*, 1764.
[33] E.T. Hoke, D.J. Slotcavage, E.R. Dohner, A.R. Bowring, H.I. Karunadasa, M.D. McGehee, *Chem. Sci.* **2015**, *6*, 613.
[34] D. McMeekin, H.J. Snaith, *Science* **2016**, *351*, 151.
[35] F. Hao, C.C. Stoumpos, R.P.H. Chang, M.G. Kanatzidis, *J. Am. Chem. Soc.* **2014**, *136*, 8094.

[36] H.-S. Kim, C.-R. Lee, J.-H. Im, K.-B. Lee, T. Moehl, A. Marchioro, S.-J. Moon, R. Humphry-Baker, J.-H. Yum, J.E. Moser, M. Grätzel, N.-G. Park, *Sci. Rep.* **2012**, *2*, 591.
[37] M.M. Lee, J. Teuscher, T. Miyasaka, T.N. Murakami, H.J. Snaith, *Science* **2012**, *338*, 643.
[38] J.M. Ball, M.M. Lee, A. Hey, H.J. Snaith, *Energy Environ. Sci.* **2013**, *6*, 1739.
[39] G.E. Eperon, V.M. Burlakov, P. Docampo, A. Goriely, H.J. Snaith, *Adv. Funct. Mater.* **2014**, *24*, 151.
[40] A. Miyata, A. Mitioglu, P. Plochocka, O. Portugall, J.T.-W. Wang, S.D. Stranks, H.J. Snaith, R.J. Nicholas, *Nat. Phys.* **2015**, *11*.
[41] M.T. Hörantner, H. Snaith, *Energy Environ. Sci.* **2017**, *10*, 1983.
[42] P. Tockhorn, P. Wagner, L. Kegelmann, J.C. Stang, M. Mews, S. Albrecht, L. Korte, *ACS Appl. Energy Mater.* **2020**, *3*, 1381.
[43] H.J. Snaith, *Energy Environ. Sci.* **2012**, *5*, 6513.
[44] S.A. Gevorgyan, J. Eggert Carlé, R. Søndergaard, T. Trofod Larsen-Olsen, M. Jørgensen, F.C. Krebs, *Sol. Energy Mater. Sol. Cells* **2013**, *110*, 24.
[45] R. Timmreck, T. Meyer, J. Gilot, H. Seifert, T. Mueller, A. Furlan, M.M. Wienk, D. Wynands, J. Hohl-Ebinger, W. Warta, R.A.J. Janssen, M. Riede, K. Leo, *Nat. Photonics* **2015**, *9*, 478.
[46] J. Tauc, R. Grigorovici, A. Vancu, *Phys. Stat. Sol* **1966**, *15*, 627.
[47] O.D. Miller, E. Yablonovitch, S.R. Kurtz, *IEEE J. Photovoltaics* **2012**, *2*, 303.
[48] J.T.-W. Wang, Z. Wang, S.K. Pathak, W. Zhang, D. DeQuilettes, F. Wisnivesky, J. Huang, P. Nayak, J. Patel, H. Yusof, Y. Vaynzof, R. Zhu, I. Ramirez, J. Zhang, C. Ducati, C. Grovenor, M. Johnston, D.S. Ginger, R. Nicholas, H. Snaith, *Energy Environ. Sci.* **2016**, *9*, 2892.
[49] J. Tong, Z. Song, D.H. Kim, X. Chen, C. Chen, A.F. Palmstrom, P.F. Ndione, M.O. Reese, S.P. Dunfield, O.G. Reid, J. Liu, F. Zhang, S.P. Harvey, Z. Li, S.T. Christensen, G. Teeter, D. Zhao, M.M. Al-Jassim, M.F.A.M. Van Hest, M.C. Beard, S.E. Shaheen, J.J. Berry, Y. Yan, K. Zhu, *Science* **2019**, *364*, 475.
[50] W. Liao, D. Zhao, Y. Yu, C.R. Grice, C. Wang, A.J. Cimaroli, P. Schulz, W. Meng, K. Zhu, R.-G. Xiong, Y. Yan, *Adv. Mater.* **2016**, *28*, 9333.
[51] W. Liao, D. Zhao, Y. Yu, N. Shrestha, K. Ghimire, C.R. Grice, C. Wang, Y. Xiao, A. Cimaroli, R.J. Ellingson, N. Podraza, K. Zhu, R.-G. Xiong, Y. Yan, *J. Am. Chem. Soc.* **2016**, *138*, 12360.
[52] R. Lin, K. Xiao, Z. Qin, Q. Han, C. Zhang, M. Wei, M.I. Saidaminov, Y. Gao, J. Xu, M. Xiao, A. Li, J. Zhu, E.H. Sargent, H. Tan, *Nat. Energy* **2019**, *4*, 864.
[53] F. Hao, C.C. Stoumpos, P. Guo, N. Zhou, T.J. Marks, R.P.H. Chang, M.G. Kanatzidis, *J. Am. Chem. Soc.* **2015**, *137*, 11445.
[54] Y. Zhou, O.S. Game, S. Pang, N.P. Padture, *J. Phys. Chem. Lett.* **2015**, *6*, 4827.
[55] M. Xiao, F. Huang, W. Huang, Y. Dkhissi, Y. Zhu, J. Etheridge, A. Gray-Weale, U. Bach, Y.B. Cheng, L. Spiccia, *Angew. Chemie - Int. Ed.* **2014**, *53*, 9898.
[56] Y. Zhou, M. Yang, W. Wu, A.L. Vasiliev, K. Zhu, N.P. Padture, *J. Mater. Chem. A* **2015**, *3*, 8178.
[57] B. Conings, A. Babayigit, M.T. Klug, S. Bai, N. Gauquelin, N. Sakai, J.T.-W. Wang, J. Verbeeck, H.-G. Boyen, H.J. Snaith, *Adv. Mater.* **2016**, *28*, 10701.
[58] M.T. Klug, R.L. Milot, J.B. Patel, T. Green, H.C. Sansom, M.D. Farrar, A.J. Ramadan, S. Martani, Z. Wang, B. Wenger, J.M. Ball, L. Langshaw, A. Petrozza, M.B. Johnston, L.M. Herz, H.J. Snaith, *Energy Environ. Sci.* **2020**, *13*, 1776.
[59] T. Leijtens, R. Prasanna, A. Gold-Parker, M.F. Toney, M.D. McGehee, *ACS Energy Lett.* **2017**, *2*, 2159.
[60] M. Konstantakou, T. Stergiopoulos, *J. Mater. Chem. A* **2017**, *5*, 11518.
[61] L.M. Herz, *ACS Energy Lett.* **2017**, *2*, 1539.
[62] M.H. Kumar, S. Dharani, W.L. Leong, P.P. Boix, R.R. Prabhakar, T. Baikie, C. Shi, H. Ding, R. Ramesh, M. Asta, M. Graetzel, S.G. Mhaisalkar, N. Mathews, *Adv. Mater.* **2014**, *26*, 7122.
[63] S.J. Lee, S.S. Shin, Y.C. Kim, D. Kim, T.K. Ahn, J.H. Noh, J. Seo, S. Il Seok, *J. Am. Chem. Soc.* **2016**, *138*, 3974.
[64] T.-B. Song, T. Yokoyama, C.C. Stoumpos, J.L. Logsdon, D.H. Cao, M.R. Wasielewski, S. Aramaki, M.G. Kanatzidis, *J. Am. Chem. Soc.* **2017**, *139*, 836.
[65] T.-B. Song, T. Yokoyama, S. Aramaki, M.G. Kanatzidis, *ACS Energy Lett.* **2017**, *2*, 897.

[66] J.M. Ball, L. Buizza, H.C. Sansom, M.D. Farrar, M.T. Klug, J. Borchert, J. Patel, L.M. Herz, M.B. Johnston, H.J. Snaith, *ACS Energy Lett.* **2019**, *4*, 2748.
[67] A.D. Awtrey, R.E. Connick, *J. Am. Chem. Soc.* **1951**, *73*, 1842.
[68] T.M. Koh, T. Krishnamoorthy, N. Yantara, C. Shi, W.L. Leong, P.P. Boix, A.C. Grimsdale, S.G. Mhaisalkar, N. Mathews, *J. Mater. Chem. A* **2015**, *3*, 14996.
[69] T. Leijtens, R. Prasanna, K.A. Bush, G. Eperon, J.A. Raiford, A. Gold-Parker, E.J. Wolf, S.A. Swifter, C.C. Boyd, H.-P. Wang, M.F. Toney, S. Bent, M.D. McGehee, *Sustain. Energy Fuels* **2018**, *2*, 2450.
[70] E.S. Parrott, T. Green, R.L. Milot, M.B. Johnston, H.J. Snaith, L.M. Herz, *Adv. Funct. Mater.* **2018**, *28*, 1802803.
[71] Z. Li, M. Yang, J.-S. Park, S.-H. Wei, J. Berry, K. Zhu, *Chem. Mater.* **2015**, *28*, 284.
[72] J.-W. Lee, D.-H. Kim, H.-S. Kim, S.-W. Seo, S.M. Cho, N.-G. Park, *Adv. Energy Mater.* **2015**, *5*, 1501310.
[73] C. Yi, J. Luo, S. Meloni, A. Boziki, N. Ashari-Astani, C. Grätzel, S.M. Zakeeruddin, U. Rothlisberger, M. Grätzel, *Energy Environ. Sci.* **2016**, *9*, 656.